ORIGINAL PAPER

Qiushi Ding · Ming Zhao® · **Jiabing Xiao · Yanan Chen · Shixi Hao · Cheng Cheng · Xiaojian Li · Zhengxian Liu**

Large eddy simulation based on an improved high-precision interior penalty discontinuous Galerkin method: flow past cylinders and airfoils

Abstract The accuracy of flow field prediction relies on the resolution of the flow structures, and numerical simulation of flow field based on high-precision methods is of great significance. To this end, an improved interior penalty discontinuous Galerkin (IPDG) method was adopted in the present study to conduct large eddy simulation (LES). It has been validated that the improved IPDG method can reach a precision of at least fourth order. Moreover, the effects of subgrid-scale models and numerical dissipation in the IPDG-LES framework remain questionable. Therefore, the turbulent flow past a circular cylinder at $Re = 3900$ has been systematically investigated. Compared with Smagorinsky models with/without a damping function and wall-adapting local eddy viscosity model, the dynamic subgrid model leads to higher accuracy due to the modeling strategy. The effect of numerical dissipation seems perverse, and the discrepancy could be attribute to the generation of aliasing error and resolved viscosity when numerical dissipation is artificially suppressed. In addition, NACA0021 airfoil flow simulation at AOA = 60 deg and $Re = 2.7 \times 10^5$ has been conducted. The characteristics of the turbulence field and high precision are also well demonstrated under the IPDG-LES framework.

1 Introduction

Within the finite volume method (FVM) framework, LES has become a powerful tool between direct numerical simulation (DNS) and Reynolds-averaged Navier–Stokes (RANS), capable of simulating vortex-dominated flow structures in many aerospace applications, such as flows over high lift configurations, rotorcraft flows and more recently flows in aircraft engines [1–5]. Actually, several improvements have been made corresponding to the original Smagorinsky model within the LES framework. For instance, the Smagorinsky model with a damping function, WALE and dynamic subgrid models have been proposed, and their pros and cons have been comprehensively discussed. For example, Arya and De [6] pointed out that the near-wall eddy viscosity profile for the WALE model was more accurate than the dynamic subgrid model in the study of backward-facing step flow. Lee and Cant [7] conducted a confined axisymmetrical bluff body flow simulation, and it was found that the Smagorinsky and WALE models were more dissipative than the dynamic subgrid model and subgrid turbulent kinetic energy (TKE) model. It was recognized that the WALE model was more suitable for the transition prediction with less computation resource requirement [8, 9]. On the other hand, the Smagorinsky, WALE and dynamic subgrid models provided almost the same results [10]. Meanwhile, the WALE and dynamic

Q. Ding · M. Zhao (✉) · J. Xiao · Y. Chen · S. Hao · C. Cheng · X. Li · Z. Liu
Department of Mechanics, School of Mechanical Engineering, Tianjin University, Tianjin 300350, China
e-mail: ming.zhao@tju.edu.cn

Z. Liu
e-mail: zxliu@tju.edu.cn

M. Zhao · X. Li · Z. Liu
Tianjin Key Laboratory of Modern Engineering Mechanics, Tianjin University, Tianjin 300350, China

subgrid models also resulted in commensurate accuracy in the simulation of Taylor–Couette–Poiseuille flows [8].

Due to the high resolution of LES method, numerical methods of high-precision, low-dissipation and low-dispersion are preferable. Although traditional FVM is well conserved and suitable for complex boundaries, it is difficult to improve the accuracy without ruining the compactness. When the grid resolution is inadequate, the SGS models are likely to be contaminated by the numerical truncation errors stemming from the lower-order numerical methods. In contrast, higher-precision methods are more compatible to the needs of delicate flow structure resolution, so the combination of LES models and high-precision numerical methods becomes an important tendency at present [11].

Recently, high-precision methods have made great progress, among which the discontinuous Galerkin method (DGM) has attracted much attention for its compactness, stability and convergence as well as the high compatibility of parallel algorithms. When the Navier–Stokes (N–S) equations are considered, several schemes have been proposed for the discretization of the viscous terms within the DGM framework. In detail, there are mainly two kinds of schemes to reduce the order of the governing equations. One takes the gradients of conserved variables as auxiliary variables. On this basis, Bassi and Rebay [12] proposed the Bassi–Rebay 1 (BR1) scheme when solving the compressible N–S equations. Then, the convergence and compactness have been improved with the Bassi–Rebay 2 (BR2) scheme [13]. However, this method is in need of auxiliary variable equations [14]. Furthermore, Cockburn and Shu [1] proposed the local discontinuous Galerkin (LDG) method, which is L^2-stable in the nonlinear case. Hartmann and Houston [2, 3] proposed an alternative method, which takes the whole viscous flux as the auxiliary variable within the IPDG framework. Different from the BR methods, no equation of auxiliary variable is introduced. Recently, an improved IPDG method has been proposed and adopted in RANS simulations in our previous studies [15]. The computation and storage of the fourth-order homogeneity tensor within the original IPDG framework has been removed, leading to improvement in algorithm and programming.

Several attempts of the combination of DGM methods and LES models have been conducted [4, 16–18]. For example, Chapelier et al. [16] discussed the influence of the LES filter scale Δ with respect to the numerical precision p and the grid size h, which results from the increase in degrees of freedom (DOF) within an element. Bassi et al. [17] proposed a p-adaptive method to perform implicit LES (ILES) simulations of circular and square cylinders, which could greatly reduce the number of DOF. Sengupta et al. [18] altered the solution from a nodal representation to a modal one for the convenience of data filtering, and performed LES simulations of channel flow using the DG spectral method. Inspired by the variational multiscale simulation (VMS) method, Abbà et al. [4] adopted a truncation method for the filtering operations in the dynamic subgrid model implementation. On this basis, a locally p-adaptive approach of LES was proposed [19], and extended to a dynamically adaptive fashion [20].

It is commonly accepted that the numerical accuracy is greatly affected by the numerical dissipation. And the overall dissipation properties of DGM are strongly determined by the convective flux scheme used for solving the discontinuity of the solution at elements interfaces [21]. For example, Winters et al. [22] studied the dissipative behavior of Roe and local Lax-Friedrichs (LLF) schemes and the instability of Taylor–Green vortex (TGV). Van der Bos and Geurts [23] found that numerical dissipation of the HLLC flux may interfere with the large eddy sub-filter scale modeling; while, it was shown that an approximate 'principle of exchange of dissipation' can be put forward. Meanwhile, the effect of the numerical flux function on the accuracy of the DGM-LES solutions has been investigated by performing ILES and VMS simulations of the TGV configuration [24]. The use of the DGM-VMS approach in combination with the least dissipative possible numerical flux led to the best match with the reference data. In addition, Nigro et al. [21] conducted simulations of inviscid flow around airfoil and TGV, etc. The benefits of using the modified dissipation appear more evident in both the averaged streamwise velocity and in the root mean square of the fluctuation.

On the other hand, it is notable that there is a risk of aliasing errors along with the increase in numerical accuracy and decrease in numerical dissipation. Theoretically, it is believed the aliasing errors stem from the under-integration of the nonlinear term within the DGM framework, since the number of quadrature points is always necessary to integrate the linear terms exactly. The complicated interaction among the truncation error, the aliasing error and the modeling error might emerge in the LES studies within the DGM framework such that it is difficult to assess the effects of numerical dissipation and aliasing error in a systematic manner. To this end, two de-aliasing rules according to the over-integration strategy were proposed with a primary drawback of increased computational cost [25]. Then, the influence of the discretization choice of the nonlinear terms on the SGS modeling in an explicit LES approach was discussed [26], where a classic Smagorinsky model and

a VMS method with a Smagorinsky viscosity were adopted. It has been found that the aliasing error would influence the solution and thus any solution-dependent quantities.

However, to our knowledge, although DGM has been utilized in cylinder and airfoil flow field simulations [5, 27, 28], the influence of SGS models has been barely discussed within the DGM-LES framework. Meanwhile, although the influences of numerical dissipation of flux schemes have been discussed in homogeneous turbulence and TGV within the DGM framework, the corresponding impacts of numerical dissipation and aliasing error are still unknown in LES study of subcritical cylinders. To this end, the present study conducts LES simulations of flows around a subcritical circular cylinder at $Re = 3900$ with the improved IPDG method and several SGS models, including Smagorinsky models with/without a damping function, WALE and dynamic subgrid models. Furthermore, the impacts of numerical dissipation of LLF scheme have been comprehensively analyzed in the cylinder wake simulations with the help of the dynamic subgrid model. It turns out that the dynamic subgrid model is superior under the current conditions. Since the subcritical cylinder flow leads to flow transition within the shear layer after flow separation, the advantages of WALE model cannot be identified. In addition, in high-precision framework, numerical viscosity can affect the modeled viscosity through the aliasing error, and then affect the numerical simulation results.

The remainder of the paper is arranged as follows. Section 2 gives the governing equations and four LES subgrid models. The improved IPDG method, the modified version of the LLF flux as well as other numerical methods are presented in Sect. 3. In Sect. 4, the method is validated in the subcritical cylinder flow at $Re = 3900$ and the results are quantitatively compared with those from the numerical and experimental references. At the same time, the effects of different SGS models and numerical dissipation are discussed in depth. The NACA0021 airfoil in deep stall is also simulated to validate the numerical accuracy and to depict the turbulence field. The concluding remarks are laid out in the last section.

2 Governing equations and LES method

2.1 Governing equations

First, far-field density ρ_∞, characteristic length L, far-field velocity u_∞, far-field temperature T_∞, and far-field dynamic viscosity μ_∞ are selected as the reference values. The dimensionless values are then labeled by the star superscript:

$$\rho^* = \frac{\rho}{\rho_\infty}, \; x_i^* = \frac{x_i}{L}, \; u_i^* = \frac{u_i}{u_\infty}, \; t^* = \frac{t}{L/u_\infty}, \; p^* = \frac{p}{\rho_\infty u_\infty^2}, \; T^* = \frac{T}{T_\infty}, \; \mu^* = \frac{\mu}{\mu_\infty}$$

For the sake of convenience, the superscript * is omitted and the dimensionless quantity could be reverted to the original form. Then, the non-dimensional compressible N–S equations are listed as follows:

$$\frac{\partial \rho}{\partial t} + \frac{\partial}{\partial x_j}\left(\rho u_j\right) = 0 \tag{1}$$

$$\frac{\partial}{\partial t}(\rho u_i) + \frac{\partial}{\partial x_j}\left(\rho u_i u_j + p\delta_{ij}\right) = \frac{\partial \sigma_{ij}}{\partial x_j} \tag{2}$$

$$\frac{\partial}{\partial t}(\rho e) + \frac{\partial}{\partial x_j}\left[(\rho e + p)u_j\right] = \frac{\partial}{\partial x_j}\left(\sigma_{jk}u_k - q_j\right) \tag{3}$$

Here, $\sigma_{ij} = \frac{\mu}{Re}\left(\frac{\partial u_i}{\partial x_j} + \frac{\partial u_j}{\partial x_i} - \frac{2}{3}\frac{u_k}{x_k}\delta_{ij}\right)$ represents the viscous stress tensor, $q_j = -\frac{\mu}{(\gamma-1)Ma^2 RePr}\frac{\partial T}{\partial x_j}$ indicates the heat flux. $Re = \frac{\rho_\infty u_\infty L}{\mu_\infty}$, $Ma = \frac{u_\infty}{\sqrt{\gamma R T_\infty}}$ and Pr denote the Reynolds number, the Mach number and the Prandtl number, respectively.

2.2 LES method

Then, the filtered N–S equations for LES simulation are introduced as follows. Applying filtering in physical space (denoted by $^-$) to each term in the N–S equations results in filtered forms of the coupling quantities, for instance, $\overline{\rho u_i u_j}$. In order to simplify the filtering process and decouple the density and pressure from the coupling quantities, the Favre filter (denoted by $^\sim$) is introduced. Take an arbitrary variable f for example, $\overline{\rho f} = \overline{\rho}\tilde{f}$, where f can represent the velocity, temperature and energy, etc.

Suppose that the filtering operation can commute with the derivation operation, that is, ignore the commutator error [4]. The following approximate relation is thus considered valid:

$$\overline{\sigma_{jk} u_k} \approx \widetilde{\sigma_{jk}} \widetilde{u}_k \tag{4}$$

$$\overline{\rho e} = \overline{\rho} \widetilde{e} \approx \frac{\overline{p}}{\gamma - 1} + \frac{1}{2} \overline{\rho} \widetilde{u}_i \widetilde{u}_i \tag{5}$$

$$\overline{\sigma_{ij}} \approx \widetilde{\sigma}_{ij} \tag{6}$$

The Favre filtered equations are obtained as follows:

$$\frac{\partial \overline{\rho}}{\partial t} + \frac{\partial}{\partial x_j} \left(\overline{\rho} \widetilde{u}_j \right) = 0 \tag{7}$$

$$\frac{\partial}{\partial t} \left(\overline{\rho} \widetilde{u}_j \right) + \frac{\partial}{\partial x_j} \left(\overline{\rho} \widetilde{u}_i \widetilde{u}_j + \overline{p} \delta_{ij} \right) = \frac{\partial \widetilde{\sigma}_{ij}}{\partial x_j} - \frac{\partial}{\partial x_j} \left(\overline{\rho u_i u_j} - \overline{\rho} \widetilde{u}_i \widetilde{u}_j \right) \tag{8}$$

$$\frac{\partial}{\partial t} \left(\overline{\rho} \widetilde{e} \right) + \frac{\partial}{\partial x_j} \left[(\overline{\rho} \widetilde{e} + \overline{p}) \widetilde{u}_j \right] = \frac{\partial}{\partial x_j} \left(\widetilde{\sigma_{jk}} \widetilde{u}_k - \widetilde{q}_j \right) - \frac{\partial}{\partial x_j} \left[\overline{\rho e u_j} + \overline{p u_j} - (\overline{\rho} \widetilde{e} + \overline{p}) \widetilde{u}_j \right] \tag{9}$$

Among them, the subgrid Reynolds stress term $\tau_{ij} = \overline{\rho u_i u_j} - \overline{\rho} \widetilde{u}_i \widetilde{u}_j$ reflects the influence of the filtered small-scale quantities on the flow field. In the last term of the energy Eq. 9, we have $\overline{\rho e u_j} + \overline{p u_j} - (\overline{\rho} \widetilde{e} + \overline{p}) \widetilde{u}_j = \frac{\gamma R}{\gamma - 1} \overline{\rho} \left(\widetilde{T u_j} - \widetilde{T} \widetilde{u}_j \right) + \frac{1}{2} \overline{\rho} (\widetilde{u_i u_i u_j} - \widetilde{u_i u_i} \widetilde{u}_j)$. $q_j^{SGS} = \overline{\rho} (\widetilde{T u_j} - \widetilde{T} \widetilde{u}_j)$ is the subgrid heat flux, and $\frac{1}{2} \overline{\rho} (\widetilde{u_i u_i u_j} - \widetilde{u_i u_i} \widetilde{u}_j) \approx \tau_{ij} \widetilde{u}_i$.

Ignoring the isotropic part of τ_{ij}, τ_{ij} and q_j^{SGS} are modeled by the eddy viscosity hypothesis. The expression of τ_{ij} varies in different SGS models and $q_j^{SGS} = -\frac{\mu_t}{Pr_t} \frac{\partial \widetilde{T}}{\partial x_j} = -\frac{C \overline{\rho} \Delta^2 |\overline{S_{ij}}|}{Pr_t} \frac{\partial \widetilde{T}}{\partial x_j}$. Where $\Delta = (\Delta x \Delta y \Delta z)^{\frac{1}{3}}$ represents the grid scale, $\left| \overline{S_{ij}} \right| = (2 \overline{S_{ij} S_{ij}})^{\frac{1}{2}}$, and the large-scale strain rate tensor is $\overline{S_{ij}} = \frac{1}{2} (\frac{\partial \widetilde{u}_i}{\partial x_j} + \frac{\partial \widetilde{u}_j}{\partial x_i})$. Pr_t is the turbulent Prandtl number, which is set to 0.9 in the present study.

2.3 SGS models

(1) The original Smagorinsky model

The Smagorinsky model based on the eddy viscosity hypothesis is a well-known subgrid model. In the original Smagorinsky model, $\tau_{ij} = -2 C \overline{\rho} \Delta^2 |\overline{S_{ij}}| \overline{S_{ij}}$. And the coefficient $C = C_S^2$ is empirically given as a constant, $C_S = 0.1$ is the Smagorinsky constant [29]. However, the parameter of the Smagorinsky model suffers from the mismatch of the asymptotic behavior of the viscous stress near walls, and should be adjusted for different conditions [30]. Meanwhile, the viscous stress produces excessive damping of resolved structures in transition, resulting in incorrect growth rate of perturbations. The Smagorinsky model with a damping function, WALE and dynamic subgrid models have been proposed to overcome the shortcomings of the original Smagorinsky model, respectively.

(2) The Smagorinsky model with a damping function

In order to recover the correct physical distribution of turbulence viscosity and ensure the turbulence viscosity decay near the wall surface, the Van Driest damping function $f_D(y^+) = 1 - \exp(-y^+/A)$ is introduced here [31]. y^+ is the dimensionless distance to the wall surface, and A is a constant, which is set to 25 in the present study. Therefore, C is revised to $C_S^2 f_D(y^+)$ in consideration of the near-wall damping correction.

(3) The dynamic subgrid model

Different from the original Smagorinsky model where C is a fixed constant, the dynamic subgrid model adopts the scale similarity hypothesis to calculate C. It is dynamically determined by the relationship between two filters of different scales. Actually, in order to determine C, a test filter (denoted by $\wedge$) is introduced. The subgrid stress is expressed as $T_{ij} = \widehat{\overline{\rho u_i u_j}} - \frac{\widehat{\overline{\rho u_i}} \, \widehat{\overline{\rho u_j}}}{\widehat{\overline{\rho}}} = \widehat{\overline{\rho u_i}} \widetilde{u}_i - \frac{\widehat{\overline{\rho u_i}} \, \widehat{\overline{\rho u_j}}}{\widehat{\overline{\rho}}} = -2 C \widehat{\overline{\rho}} \widehat{\Delta}^2 \left| \widehat{\overline{S}}_{ij} \right| \widehat{\overline{S}}_{ij}$ after the test filtering, and the Lonard stress tensor $L_{ij} = T_{ij} - \widehat{\tau}_{ij} = \widehat{\overline{\rho} \widetilde{u}_i \widetilde{u}_j} - \frac{\widehat{\overline{\rho u_i}} \, \widehat{\overline{\rho u_j}}}{\widehat{\overline{\rho}}}$ given by the Germano identity [32] is obviously a known quantity. Therefore, C could be determined by the least-square method. In addition, it is worth noting

that for unstructured grids, the expression of grid scale is difficult to determine. Nevertheless, provided the relationship between the test filter scale and the grid scale $\widehat{\Delta} = 2\Delta$, $\frac{\widehat{\Delta}^2}{\Delta^2} = 4$ is obtained immediately. In order to avoid explicitly specifying the grid filtering scale, $C\Delta^2 = \frac{L_{ij}(A_{ij} - \widehat{B_{ij}})}{(A_{kl} - \widehat{B_{kl}})(A_{kl} - \widehat{B_{kl}})}$ is calculated here [18], where $A_{ij} = -2\widehat{\overline{\rho}}\frac{\widehat{\Delta}^2}{\Delta^2}\left|\widehat{\overline{S_{ij}}}\right|\widehat{\overline{S_{ij}}}$ and $B_{ij} = -2\overline{\rho}\left|\overline{S_{ij}}\right|\overline{S_{ij}}$. Actually, the quantities after the test filtering process are obtained through the truncation method in accompany with the DGM discretization process [4], which could also be regarded as a L^2 projection process.

(4) The WALE model

The asymptotic behavior toward the wall in the original Smagorinsky model can also be corrected by the WALE model. The WALE model takes into account both the rotation and strain rates; whereas, the Smagorinsky model only takes into account the deformation rate of the turbulent structure [33]. It can reproduce the transition process from laminar flow to turbulent flow and obtain the correct wall asymptotic law of the eddy viscosity. The modeling of subgrid Reynolds stress term is based on a tensor invariant of velocity gradient [34], $\tau_{ij} = \overline{\rho}\left(C_W\frac{\Delta}{(p+1)}\right)^2 \frac{\left(S_{ij}^d S_{ij}^d\right)^{\frac{3}{2}}}{\left(\overline{S_{ij}}\,\overline{S_{ij}}\right)^{\frac{5}{2}} + \left(S_{ij}^d S_{ij}^d\right)^{\frac{5}{4}}}\overline{S_{ij}}$. Where $\overline{S_{ij}}^d = \frac{1}{2}\left(\overline{g}_{ij}^2 + \overline{g}_{ji}^2\right) - \frac{1}{3}\delta_{ij}\overline{g}_{kk}^2$, $\overline{g}_{ij}^2 = \overline{g}_{ik}\overline{g}_{kj}$, $\overline{g}_{ij} = \frac{\partial \widetilde{u}_i}{\partial x_j}$. C_W represents the model constant, which is set to 0.6 in the present study. And p is a polynomial order [35].

3 Numerical methods and validation

As mentioned above, an improved IPDG method is adopted in the present study for the spatial discretization of N–S equations. Starting from Eqs. 7–9 in vector form:

$$\partial_t U + \nabla \cdot \left(F^c + F^v\right) = 0 \tag{10}$$

where F^c and F^v stand for the convection term and the viscous term, $g(U)$ is the homogeneity tensor describing the relationship between the viscous term and the variable gradient. The viscous flux is then written in the form of the double-dot product of the homogeneity tensor and the gradient of the conserved variable, that is $\Theta = F^v(U, \nabla U) = g(U) : \nabla U$. Unlike the BR methods, which take the gradients of the conserved variable as the auxiliary variables to calculate the viscous term, the IPDG method takes the whole viscous flux as the auxiliary variable. Moreover, the improved IPDG method here attempts not to calculate the fourth-order homogeneity tensor.

Then, multiply Eq. 10 by the test function φ and integrate by parts according to DGM:

$$\int_\Omega \partial_t U \cdot \varphi \mathrm{d}V + \int_{\partial\Omega} \left(\widehat{F^c} + \widehat{F^v}\right) \cdot \varphi \mathrm{d}S - \int_\Omega F^c : \nabla\varphi \mathrm{d}V - \int_\Omega \Theta : \nabla\varphi \mathrm{d}V = 0 \tag{11}$$

To pursue the high-precision characteristics, it is necessary to recast the last term individually and carry out integral by parts again. The specific process is as follows:

$$\begin{aligned}
\int_\Omega \Theta : \nabla\varphi \mathrm{d}V &= \int_\Omega (g : \nabla U) : \nabla\varphi \mathrm{d}V = \int_\Omega \nabla U : \left(g^T : \nabla\varphi\right)\mathrm{d}V \\
&= \int_{\partial\Omega} U \otimes \vec{n} : \left(g^T : \nabla\varphi\right)\mathrm{d}S - \int_\Omega U : \nabla \cdot \left(g^T : \nabla\varphi\right)\mathrm{d}V \\
&= \int_{\partial\Omega} g : \hat{U} \otimes \vec{n} : \nabla\varphi \mathrm{d}S - \int_\Omega U : \nabla \cdot \left(g^T : \nabla\varphi\right)\mathrm{d}V \\
&= \int_{\partial\Omega} g : \hat{U} \otimes \vec{n} : \nabla\varphi \mathrm{d}S - \left(\int_{\partial\Omega} g : U \otimes \vec{n} : \nabla\varphi \mathrm{d}S - \int_\Omega \nabla U : \left(g^T : \nabla\varphi\right)\mathrm{d}V\right) \\
&= \int_{\partial\Omega} g : \left(\hat{U} - U\right) \otimes \vec{n} : \nabla\varphi \mathrm{d}S + \int_\Omega F^v : \nabla\varphi \mathrm{d}V
\end{aligned} \tag{12}$$

Therefore, Eq. 11 can be further written as:

$$\int_\Omega \partial_t U \cdot \varphi dV + \int_{\partial\Omega} \left(\hat{F}^c + \hat{F}^v \right) \cdot \varphi dS - \int_\Omega (F^c + F^v) : \nabla\varphi dV - \int_{\partial\Omega} g : \left(\hat{U} - U \right) \otimes \vec{n} : \nabla\varphi dS = 0 \quad (13)$$

In the above formula, the convection flux $\widehat{F}^c$, viscous flux $\widehat{F}^v$ and variable flux $\widehat{U}$ need to be individually specified. In addition, in order to eliminate the influence of the homogeneity tensor, efforts should be made to recast the lifting operator term $L =$ according to the viscous term $F^v(U, \nabla U) = g(U) : \nabla U$. In the original IPDG method, $\hat{U} = \frac{1}{2}(U^+ + U^-)$ is the variables flux, $()^+$ and $()^-$ represent the left and right limitations at the interface.

As a result, the final form of N–S equation can be obtained by the improved IPDG method:

$$\int_\Omega \partial_t U \cdot \varphi dV + \int_{\partial\Omega} \left(\hat{F}^c + \hat{F}^v \right) \cdot \varphi dS - \int_\Omega (F^c + F^v) : \nabla\varphi dV + \int_{\partial\Omega} L : \nabla\varphi dS = 0 \quad (14)$$

The lifting operator is rewritten as follows, analogous with the expression of the viscous term:

$$L = F^v \left(\frac{1}{2}(U^+ + U^-), \frac{1}{2}(U^+ - U^-) \otimes \vec{n} \right) \quad (15)$$

$$\hat{F}^v = \frac{1}{2} \left(F^v(U^+, \nabla U^+) + F^v(U^-, \nabla U^-) \right) \cdot \vec{n} - C_{\text{IP}} \frac{p^2}{h_f} L \cdot \vec{n} \quad (16)$$

The penalty factor C_{IP} is a constant, p is a polynomial order, and h_f represents the scale of the surface. To calculate the convection flux and evaluate the influence of numerical dissipation, a modified version of the LLF flux [36] was adopted in the present study. To explicitly control the numerical dissipation, the LLF flux is recast into the following form, including the symmetric part and the numerical dissipation part. A parameter $\phi \in [0, 1]$ is introduced here. For the original LLF flux, $\phi = 1.0$. The smaller the value of ϕ is, the less numerical dissipation the flux scheme gets, which is closer to the central scheme. In practice, $\phi = 0.6$, 0.8 and 1.0 have been considered in the discussion of the influence of numerical dissipation. Where $\lambda_{\max} = \frac{1}{2}(\lambda^+ + \lambda^-) = \frac{1}{2} \left(\left| \vec{q}^+ \cdot \vec{n}^+ \right| + c^+ + \left| \vec{q}^- \cdot \vec{n}^- \right| + c^- \right)$, $\vec{q}$ and c denote the velocity vector and the sound velocity.

$$\hat{F}^c = \frac{1}{2} \left(F^c(U^+) + F^c(U^-) \right) \cdot \vec{n} + \phi\lambda_{\max}(U^+ - U^-) \quad (17)$$

In addition, the first term in Eq. 14 needs to be discretized in time. In this paper, the Newton–Krylov implicit method was used for time marching. It could be divided into three steps: the first step is the implicit time marching, where second-order BDF method was adopted; Then, the Newton's method was adopted to solve the nonlinear equations; Eventually, the Krylov subspace methods (e.g., the Generalized Minimal Residual (GMRES) method) was adopted to solve the linear equations within every step of the Newton iteration.

The above methodology has been comprehensively validated through inviscid and viscous cases in [15]. Among them, the laminar plate boundary layer was simulated to validate the numerical accuracy of viscous flows, which is briefly introduced here. The computational mesh is demonstrated in Fig. 1, which covers a computational domain of $[-0.5, 1] \times [0, 1]$. The lower boundary from -0.5 to 0 was set as an inviscid wall; while, the rest of the lower boundary was set as a no-slip and adiabatic wall. There are 61×60 grids within the mesh with a streamwise refinement in the vicinity of $x = 0$. The Mach number of the incoming velocity is 0.5.

The numerical accuracy has been validated from two aspects, i.e., the velocity profile and the skin friction. The velocity profiles at different streamwise locations are illustrated in Fig. 2, including $x = 0.1$, $x = 0.5$ and $x = 0.9$. The coincidence between the Blasius solution and our simulation could be clearly observed. On the other hand, the streamwise distribution of the skin friction is illustrated in Fig. 3. The coincidence between the Blasius and numerical solutions could confirm the accurate description of the velocity gradient at wall surface. The enlarged view of the skin friction at the leading-edge is also shown in Fig. 3b with logarithmic coordinates. Please refer to our previous article for more details [15].
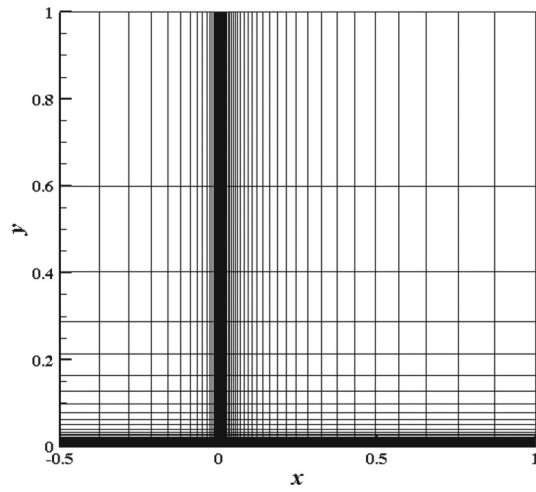
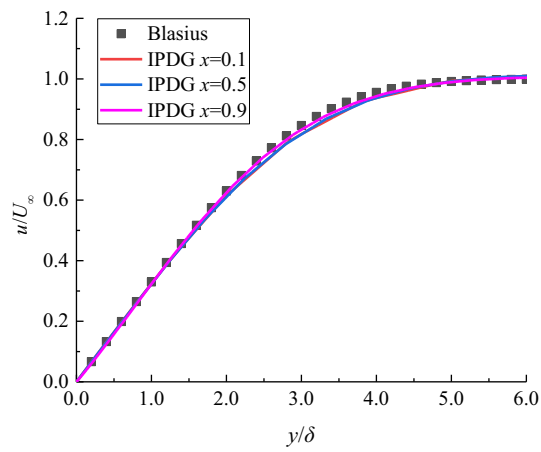**Fig. 1** Computational mesh of the plate boundary layer

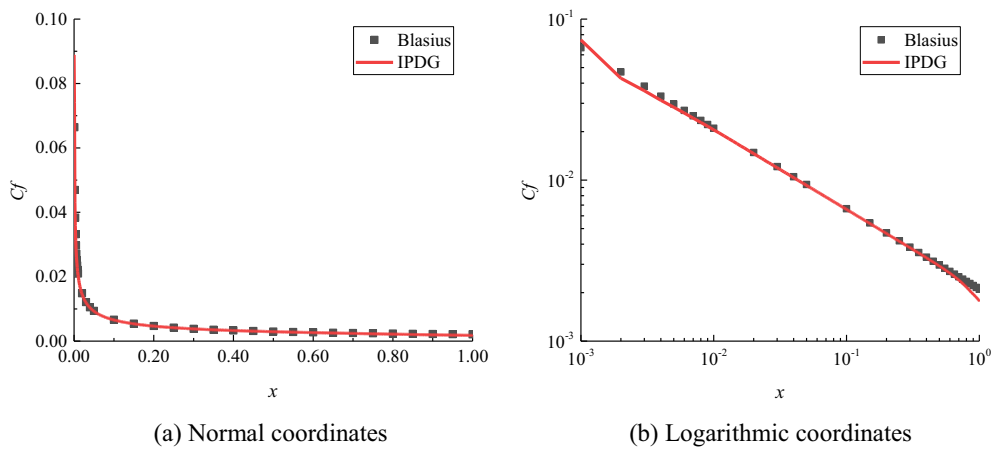**Fig. 2** Velocity profiles at different streamwise locations

(a) Normal coordinates   (b) Logarithmic coordinates

Fig. 3 Streamwise distribution of the skin friction

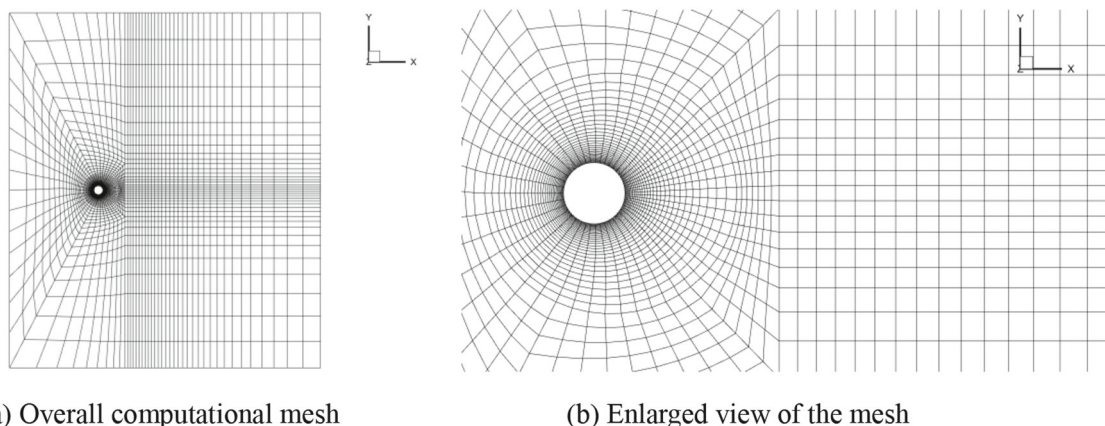(a) Overall computational mesh   (b) Enlarged view of the mesh

Fig. 4 Sketches of the cylinder mesh

4 Results and analyses

4.1 The influence of SGS models

Flow past a subcritical circular cylinder is analyzed quantitatively to validate the accuracy of the present methodology. From the physical aspect, shear layer, flow transition and separation coexist upon the cylinder surface and large-scale vortex shedding process exists in the near wake region. Therefore, it is always taken as the test case of numerical method validation [37].

As described above, the diameter of the cylinder (D) and the freestream flow velocity (u_∞) were selected as the characteristic length and the reference velocity in the present study. The fourth-order IPDG method and LES subgrid models were utilized to simulate the flowfield around a three-dimensional cylinder at $Re = 3900$ and $Ma = 0.2$. A structured mesh system was constructed within the computational domain ($-10D \leq x \leq 25D$, $-20D \leq y \leq 20D$, $-\pi D/2 \leq z \leq \pi D/2$), where x, y and z represent the streamwise, transverse and spanwise directions, respectively. The center of the cylinder was set as the origin. In detail, 16 points were equally distributed in the spanwise direction and periodic boundary conditions were imposed on the lateral surfaces. There are 50 points in the circumferential direction, among which the wake area has been refined to depict the unsteady vortex shedding process. The no-slip wall boundary condition was imposed on the cylinder surface, and 30 layers of body-fitted grids were generated. The height of the first layer is $0.01D$, corresponding to $y^+ \approx 3$, as shown in Fig. 4. It can meet the DGM's requirement of the mesh resolution [4]. As a result, the total number of grid elements is 49,755. In order to eliminate the time-marching error, the implicit second-order backward difference scheme was used. To resolve the delicate flow structures within a vortex shedding period, a non-dimensional time step of $\Delta t = 0.005$ was selected.

In this subsection, the Smagorinsky models with/without a damping function, WALE and dynamic subgrid models were tested in the subcritical cylinder simulations with the original LLF scheme ($\phi = 1.0$). In practice, physical information within 10 vortex shedding cycles have been collected in the present study.

The mean pressure coefficient ($C_p = \frac{2(\overline{p} - p_\infty)}{u_\infty^2}$) on the surface of the cylinder is plotted in Fig. 5, where $\theta = 0°$ indicates the stagnation position. Reasonable pressure distributions have been obtained compared with the experimental data [38] and numerical results, where LES and ILES were adopted [39–41]. There is no statistical difference among the Smagorinsky models with/without a damping function and WALE model. The best agreement with the reference data is achieved by the dynamic subgrid model. In detail, the result obtained by the dynamic subgrid model shows better performances compared with the ILES result from Gao et al. [39] in terms of peak value and pressure recovery. Meanwhile, it is generally analogous with those from Meyer et al. [40] with a slight improvement around $\theta = 70°$. The LES result from Rajani et al. [41] leads to the best accuracy at $\theta = 180°$. Different from the other studies, they underestimated the peak value.

It is notable that discrepancies have also been observed in the DGM-LES results in [42]. On the contrary, the DGM-VMS results lead to better coincidence with the experimental data, which could be attributed to the modeling strategy of smaller scales.

Then, some other parameters are also quantitatively compared with the references, including $C_{p,b}$, S_t and l_r. In detail, the base coefficient ($C_{p,b}$) can be evaluated as the pressure coefficient (C_p) at $\theta = 180°$.
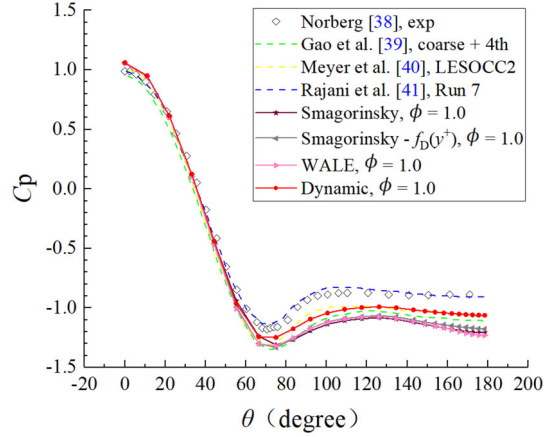
Fig. 5 Effect of SGS models on C_p distributions

**Table 1** Flow quantities in the cylinder flow simulations

Case	S_t (%)	l_r/D (%)	$-C_{p,b}$
Fröhlich et al. [45], LRUN2	0.210	1.09	1.06
Kravchenko and Moin [46], Case6	0.206	1.04	0.98
Rajani et al. [41], Run2	0.195	1.06	1.07
Rajani et al. [41], Run7	0.210	1.20	0.90
Smagorinsky, $\phi = 1.0$	0.191 (-7.28^*)	0.86 (-17.31^*)	1.21
Smagorinsky-$f_D(y^+)$, $\phi = 1.0$	0.195 (-5.34^*)	0.91 (-12.50^*)	1.18
WALE, $\phi = 1.0$	0.195 (-5.34^*)	0.91 (-12.50^*)	1.23
Dynamic, $\phi = 1.0$	0.195 (-5.34^*)	1.02 (-1.92^*)	1.06
Dynamic, $\phi = 0.8$	0.197 (-4.37^*)	0.86 (-17.31^*)	1.24
Dynamic, $\phi = 0.6$	0.200 (-2.91^*)	0.82 (-21.15^*)	1.32

*Percentages of differences based on [46]

Meanwhile, the vortex shedding Strouhal number (S_t) and the mean recirculating bubble length (l_r) are also obtained. Here, l_r represents the distance between the location of the minimum time-averaged streamwise velocity and the cylinder center. They are summarized in Table 1. Furthermore, Fig. 6 demonstrates the mean streamwise velocity distributions at different streamwise positions within the wake region, compared with the experimental data [43, 44] and numerical results [39–41]. These results suggest that there is little improvement by the Smagorinsky model with a damping function and WALE model concerning with the overdissipation in the original Smagorinsky model, since the above modifications mainly focus on the boundary layer behaviors. They generally lead to lower $C_{p,b}$, smaller l_r and velocity deficit in the near wake region. On the other hand, the velocity deficit and wake recovery have been precisely simulated by the dynamic subgrid model.

It indicates that the unsteady fluctuations and flow separation have also been accurately captured. In addition, distributions of mean transverse velocity $\langle v \rangle$ and Reynolds shear stress $\langle u'v' \rangle$ are plotted in Figs. 7 and 8. Apart from the distribution of $\langle v \rangle$ in the vicinity of $(x/D, y/D) = (1.06, 0.2)$, SGS models exhibit a good consistency. Then, the streamwise Reynolds stress $\langle u'u' \rangle$ (Fig. 9) and transverse Reynolds stress $\langle v'v' \rangle$ (Fig. 10) are also plotted. It is clearly that except the dynamic subgrid model, the other models overpredict the peak values. Although discrepancy exists in the prediction of $\langle u'u' \rangle$ from dynamic subgrid model within the far wake region, the dynamic model has the best overall performance. At the same time, the accuracy of the current numerical methods and the advantages of the dynamic subgrid model could be clearly observed.

At the plane of $z = 0$, the instantaneous contours of μ_{SGS}/μ are shown in Fig. 11, when $\phi = 1.0$. They indicate that the LES subgrid models mainly act in the wake region, where the alternate vortex shedding exists. Actually, laminar flow separation takes place and flow transition emerges in the near wake region due to K-H instability. Similar distributions are obtained by the Smagorinsky model and its modification, since the near-wall damping could not affect the wake development under the subcritical condition. In addition, the dynamic subgrid model provides the highest peak value of the SGS viscosity; while, the SGS viscosity stays around the vortex cores due to the introduction of the tensor invariant when the WALE model is adopted. The maximum
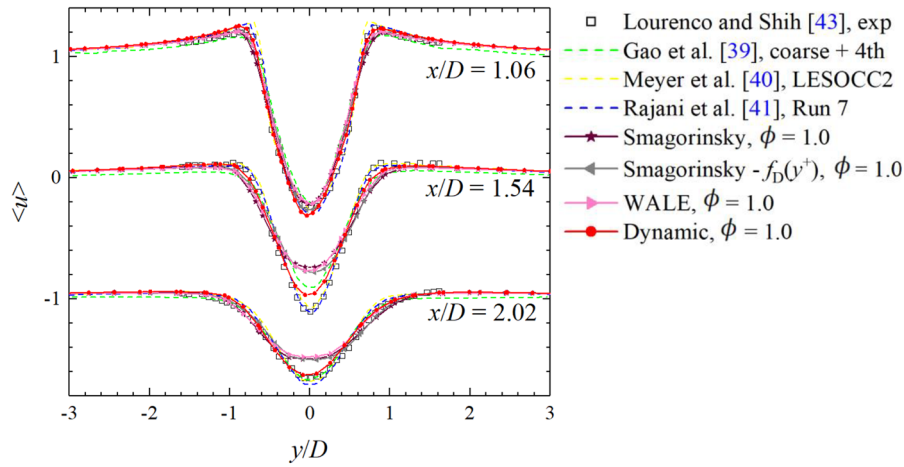
(a) In the near wake region
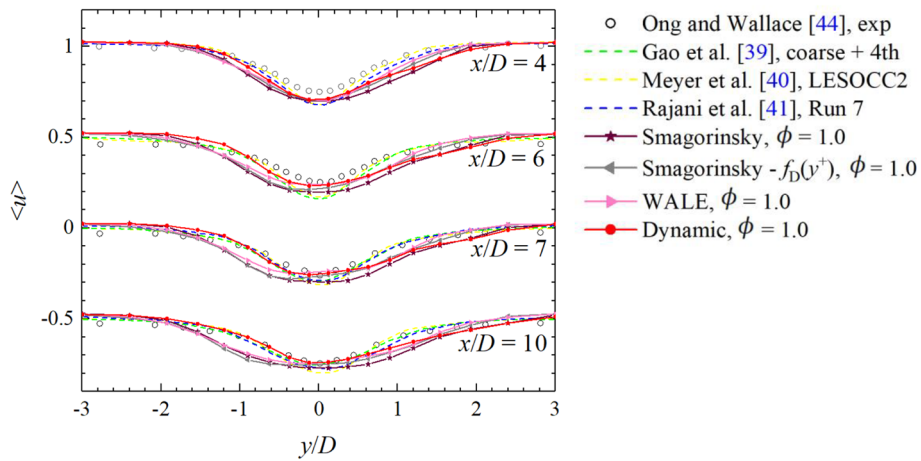
(b) In the far wake region

Fig. 6 Effect of SGS models on mean streamwise velocity at different locations
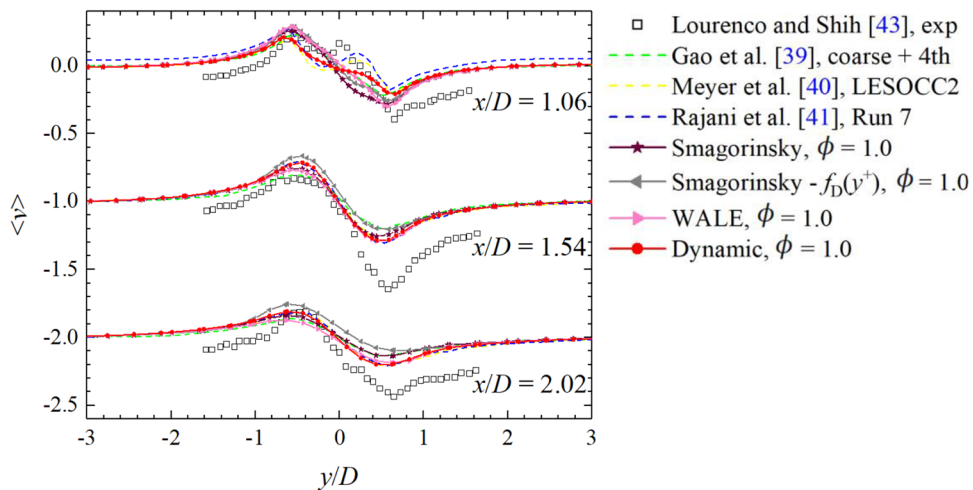

Fig. 7 Effect of SGS models on mean transverse velocity in the wake region
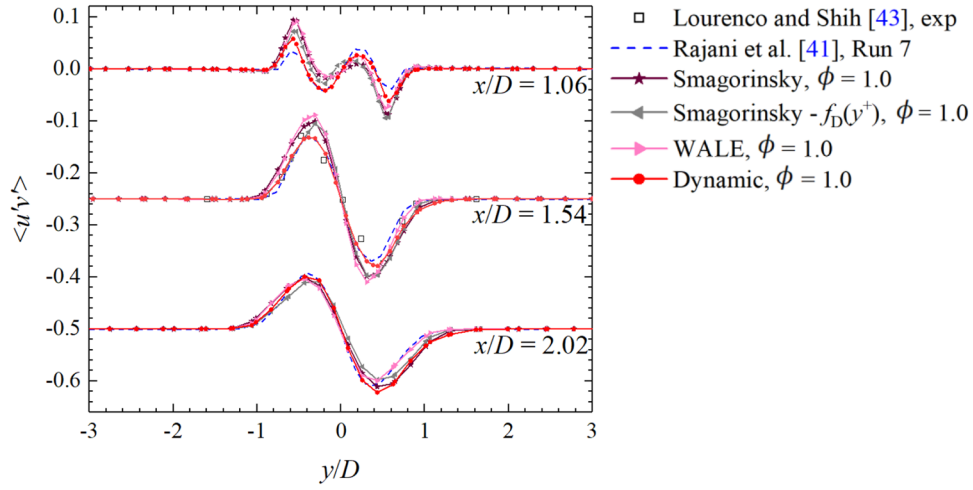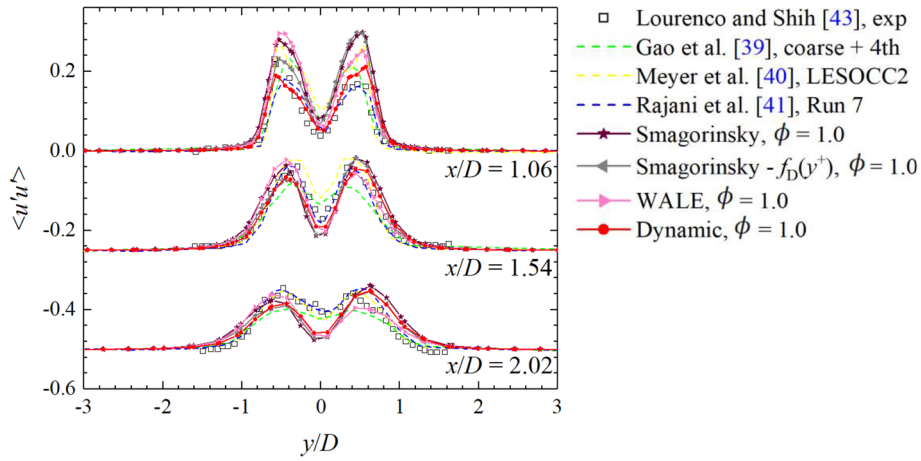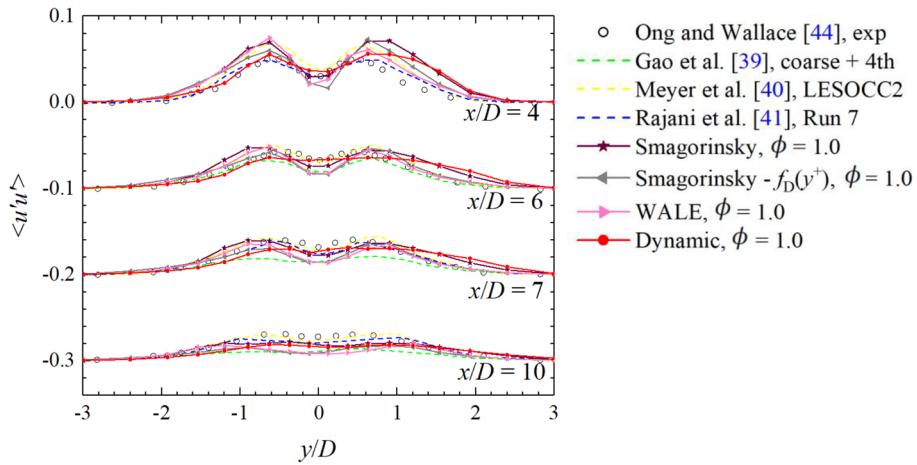
Fig. 8 Effect of SGS models on Reynolds shear stress in the wake region

(a) In the near wake region

(b) In the far wake region

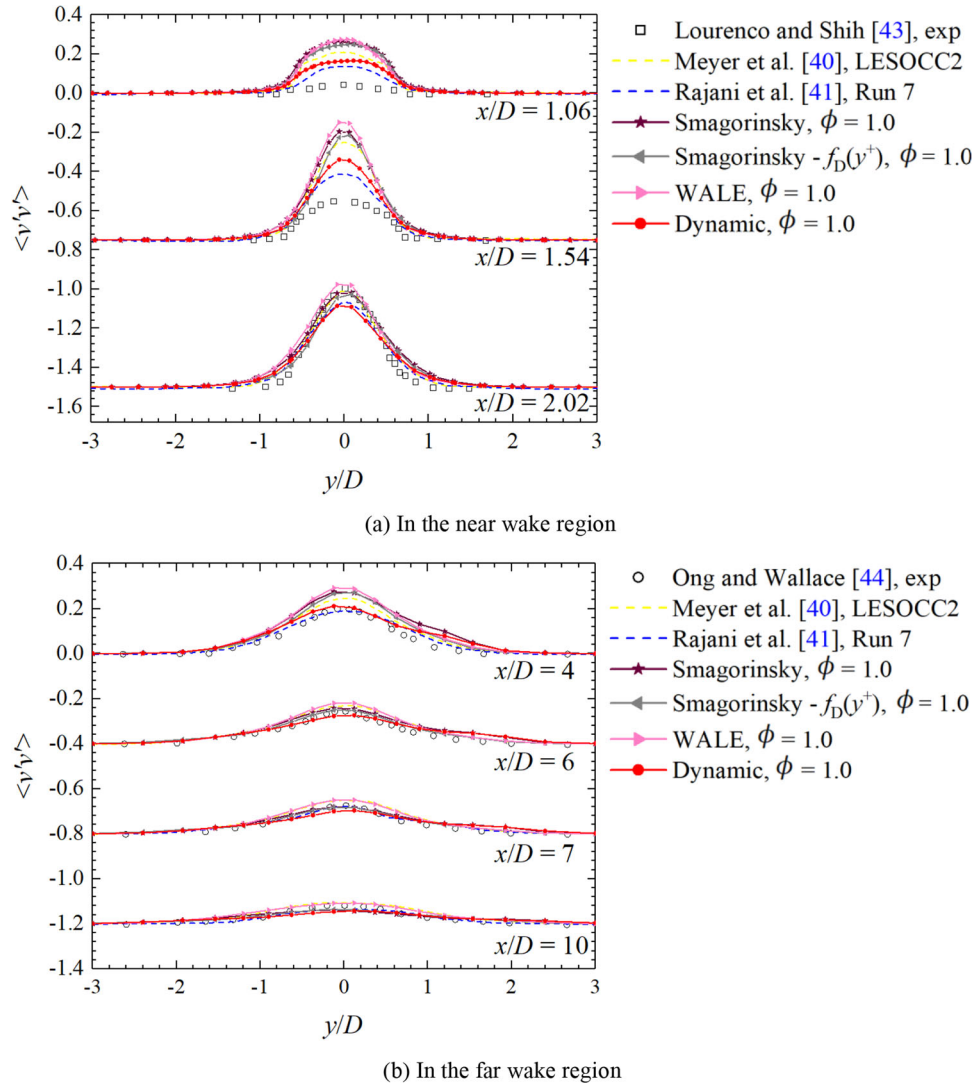**Fig. 9** Effect of SGS models on streamwise Reynolds stress at different locations

(a) In the near wake region

(b) In the far wake region

Fig. 10 Effect of SGS models on transverse Reynolds stress at different locations

values of μ_{SGS}/μ are of the order of 10 for all models, which is similar with the description of Ouvrard et al. [42].

Furthermore, the streamwise velocity at the point $x/D = 1.0$, $y/D = 0.3$ has been recorded. The streamwise velocity spectrum obtained by Fourier transform is plotted in Fig. 12. It is evident that the main peak frequency coincides with S_t in Table 1, indicating that the unsteady features are dominated by the vortex shedding process. On the other hand, a relatively smooth process of energy attenuation could be observed within the high-frequency regime, which is in alignment with the findings of Ferrer [47]. Oscillation was more obvious at high frequency in the Smagorinsky model result. Overall, the dynamic subgrid model gives the best turbulence characteristics in terms of the energy decay rate and high-frequency fluctuations.

4.2 The effect of numerical dissipation

In addition, besides the influence of SGS models, the results are also affected by truncation and aliasing errors. Therefore, it is also worth paying attention to how the numerical dissipation stemming from the spatial discretization affects the results of the N–S equations. Corresponding studies have been comprehensively conducted within the finite difference method (FDM) and FVM frameworks. For example, Chow and Moin [48] analyzed the discretization and aliasing errors induced by numerical schemes. Klein et al. [49] investigated

(a) Original Smagorinsky model

(b) Smagorinsky model with a damping function

(c) WALE model

(d) Dynamic subgrid model
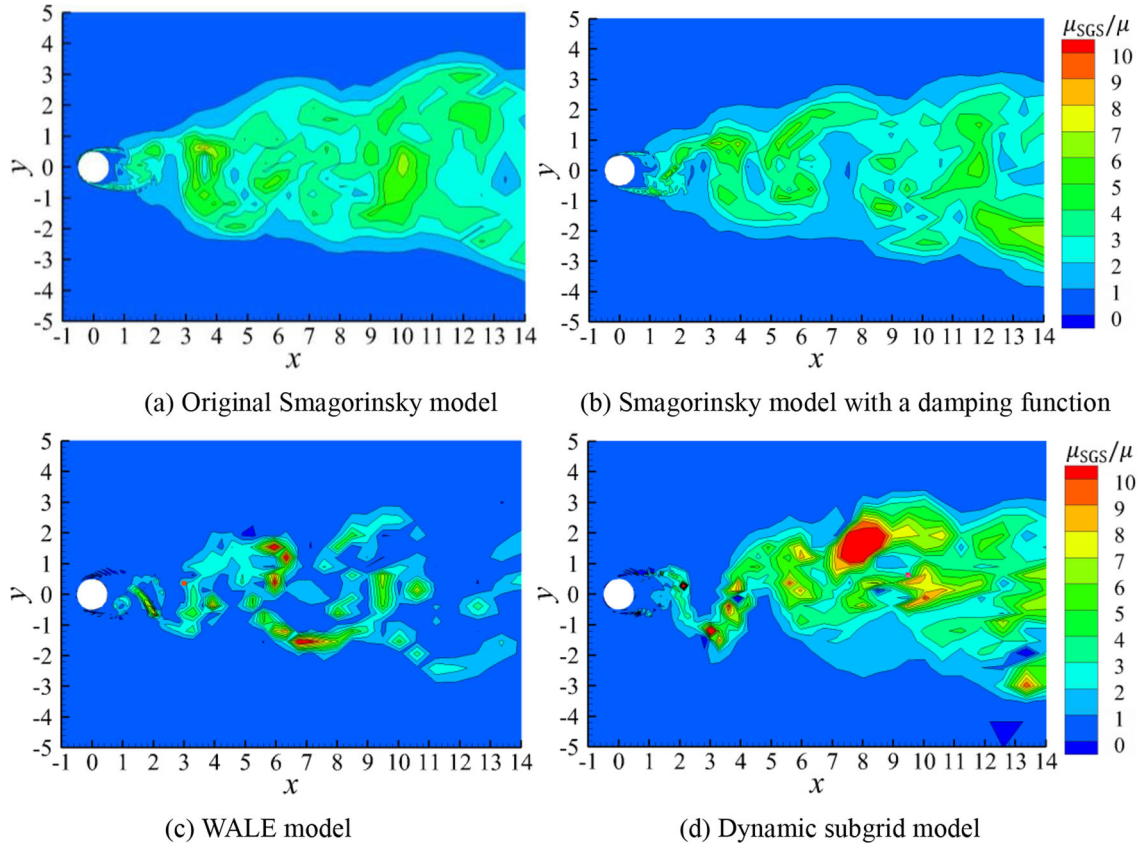
Fig. 11 Instantaneous contours of $\frac{\mu_{\mathrm{SGS}}}{\mu}$
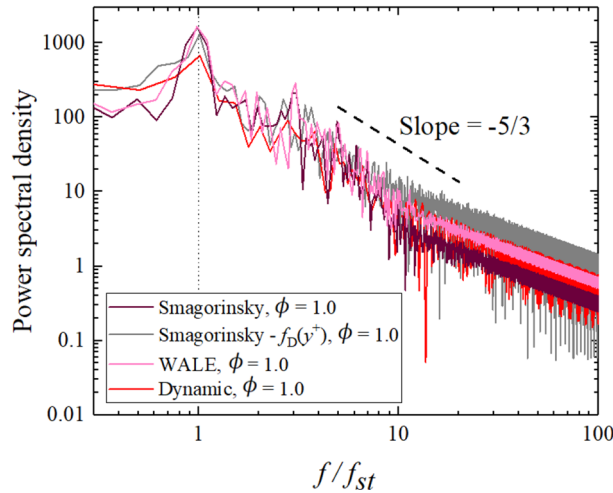
Fig. 12 Streamwise velocity spectrum (the cylinder wake simulation)

the turbulent viscosity with respect to a changing filter width and pointed out that numerical error and modeling error would interact. In general, the results are determined by the truncation error, the aliasing error and the modeling error in a complicated manner, which is difficult to be decoupled.

According to Sect. 3, three cases of $\phi = 1.0$, 0.8 and 0.6 are considered in the adjustment of LLF scheme, and obviously the numerical dissipation decreases in sequence. The dynamic subgrid model was adopted for the cylinder flow simulations. The boundary conditions, mesh resolution, numerical precision and time step

(a) $\phi = 1.0$ (b) $\phi = 0.8$ (c) $\phi = 0.6$
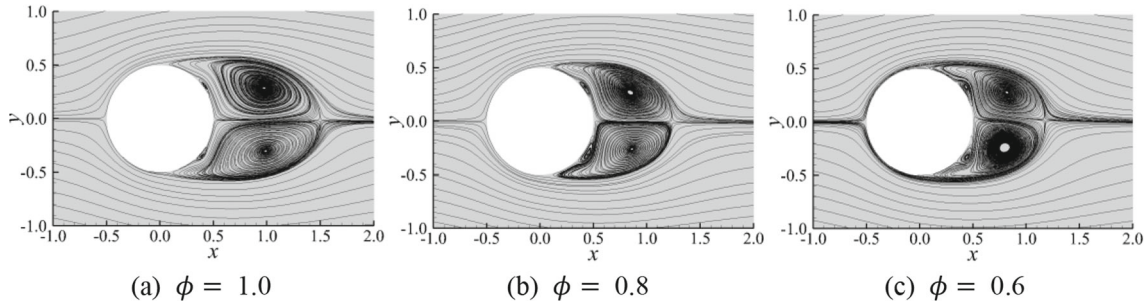
Fig. 13 Streamlines of the time-averaged flow field

(a) $\phi = 1.0$ (b) $\phi = 0.8$ (c) $\phi = 0.6$
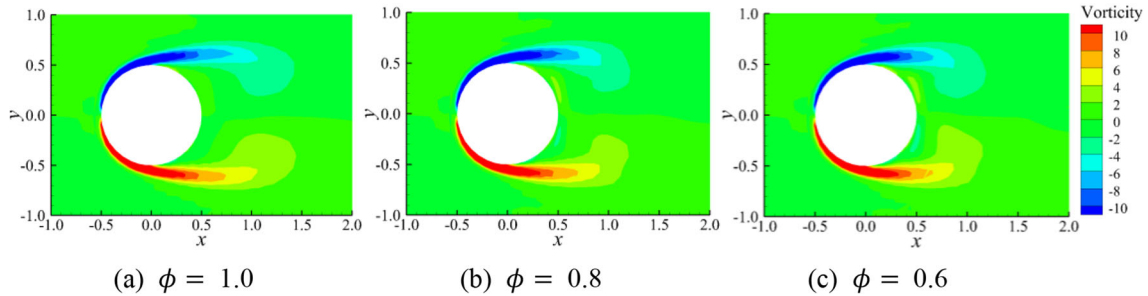
Fig. 14 Contours of the time-averaged spanwise vorticity

remains unchanged with the above subsection. The results of 10 vortex shedding cycles are also included, and the performances in the three cases can be obtained from Table 1.

As mentioned above, complicated flow phenomena emerge in the subcritical process. In detail, adverse pressure gradient will trigger flow separation in accompany with the effects of viscosity. Then, flow instability emerges within the shear layer due to K–H instability and flow transition takes place in the near wake region. Periodic vortex shedding process could be observed at the current *Re*. The time-averaged streamlines can be observed in Fig. 13. A pair of primary symmetrical vortices could be distinguished as the major flow feature. It is interesting that the recirculating bubble length (l_r) varies along with the numerical dissipation. In detail, the length monotonically increases when the numerical dissipation increases, as indicated in Table 1.

Additionally, the lengths of the shear layer can be detected by the contours of the time-averaged spanwise vorticity [50] (Fig. 14). Compared with the $\phi = 1.0$ case, $\phi = 0.6$ and $\phi = 0.8$ lead to a shorter shear layer. From the recirculating bubble length in Table 1 and the mean streamwise velocity distribution along the centerline (Fig. 15), the average velocity value of $\phi = 1.0$ scheme is slightly larger compared with its low-dissipation counterparts, and the shear layer profile is in good agreement with the reference data. It can be identified that l_r of $\phi = 0.6$ and $\phi = 0.8$ are shorter than that of the experiment. This implies a smaller recirculation, with an early transition in the near wake region.

Meanwhile, it is shown that the scheme with less numerical dissipation leads to greater overall viscosity. In detail, the distributions of the Reynolds stress components are shown in Fig. 16. The resolved viscosity of $\phi = 0.6$ and $\phi = 0.8$ schemes is obviously higher than that of $\phi = 1.0$, especially in the near wake region. This could be attributed to the increase in fluctuations caused by decreased numerical dissipation. As a result, intense momentum exchange across the shear layer emerges, which leads to a shortened recirculating bubble length.

An explanation of the above phenomenon is inherently associated with the aliasing error. In detail, since a fourth-order DGM was adopted in the present study, which leads to low numerical dissipation. Therefore, the aliasing error could probably develop without the suppression of numerical dissipation. After a long period of accumulation, the aliasing error might blur the flow field and cause shorter recirculating length. There are generally two methods to remedy this problem. One is the reduction of DGM order, which is questionable. The other is the de-aliasing method according to the over-integration strategy, which leads to an increase in computational cost. To this end, Meyers [51] analyzed the counteraction between that the modeling and discretization errors, and suggested that a priori prediction might be necessary.
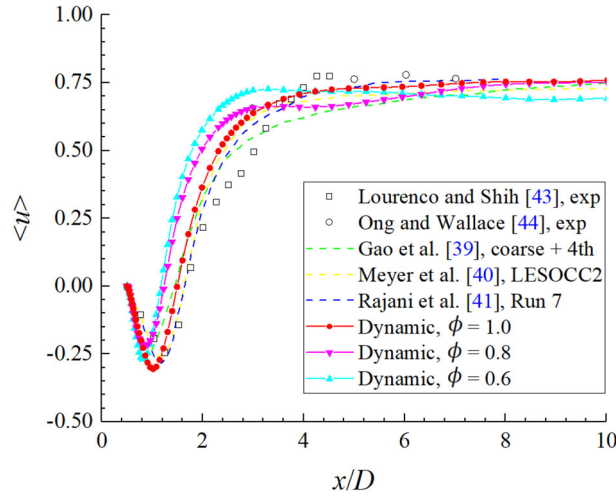
Fig. 15 Mean streamwise velocity distributions in the wake centerline
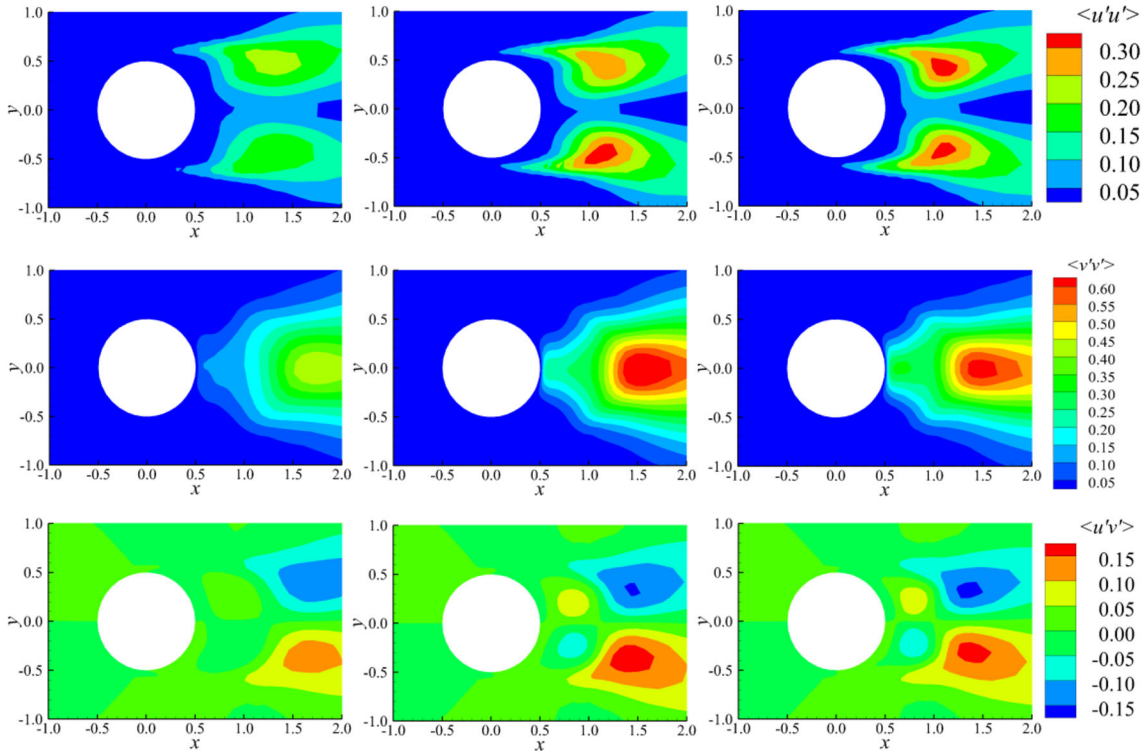

Fig. 16 Distribution of the resolved Reynolds stress components. (top: $\langle u'u' \rangle$; middle: $\langle v'v' \rangle$; bottom: $\langle u'v' \rangle$). (left: $\phi = 1.0$; middle: $\phi = 0.8$; right: $\phi = 0.6$)

According to the distribution of C_p along the cylinder surface as shown in Fig. 17, the $\phi = 0.6$ and $\phi = 0.8$ schemes overpredict the suction peak and $C_{p,b}$ as indicated in Table 1. Actually, the pressure coefficients of all the three cases deviate from -1.0 at $\theta = 180°$, consistent with the LES results in [42]. This indicates an earlier onset of flow separation along with the excessive overall viscosity. It could be directly attributed to the appearance of the secondary bubbles, which can be clearly observed in Fig. 13. The appearance of the secondary vortex means there are more separation angles within the flow field [52]. Actually, the formation and development of the secondary vortex structures are related with the interactions between the shedding vortices and the boundary layer. As mentioned above, compact shear layers are achieved with smaller l_r when
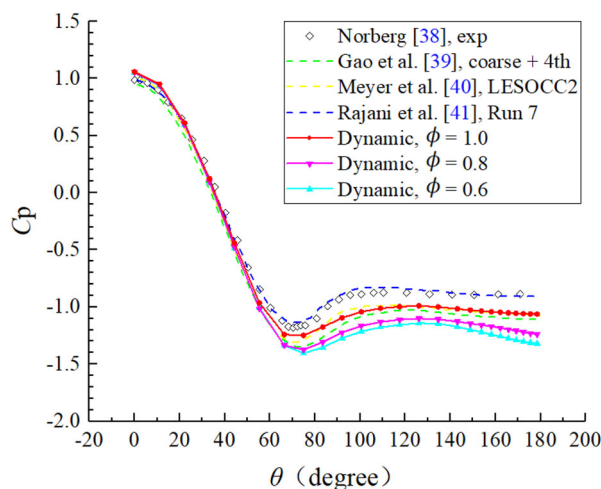
Fig. 17 Effect of numerical dissipation on C_p distributions

$\phi = 0.6$ and $\phi = 0.8$. Therefore, the interactions between the primary wake vortices and the boundary layer are more significant, leading to remarkable secondary vortices and early onset of flow separation.

Then, the wake characteristics are analyzed in detail. The mean streamwise velocity profiles at several locations (Fig. 18) can reflect the deficit and recovery in the wake region. Different mechanisms dominate in the near wake and far wake regions. In the near wake region ($x/D = 1.06$, 1.54, and 2.02), the excessive overall viscosity of $\phi = 0.6$ and $\phi = 0.8$ schemes enlarge the deviation of velocity deficit. In the far wake region ($x/D = 4$, 6, 7, and 10), the influence of resolved eddy viscosity becomes attenuated. The prediction accuracy of velocity deficit is thus improved in the case of $\phi = 0.6$ with lower numerical dissipation.

From the perspective of mean transverse velocity distributions in Fig. 19, there is little difference among the three cases of $\phi = 1.0$, 0.8 and 0.6, except for $x/D = 1.06$. The local extrema around $x = 0.2$ are not obvious in the case of $\phi = 1.0$; while, they are smeared in the cases of $\phi = 0.8$ and 0.6. It can also be observed from Fig. 20 that the Reynolds shear stress $\langle u'v' \rangle$ is well predicted in the $\phi = 1.0$ case. Actually, several local extrema have been captured at $x/D = 1.06$, consistent with the result of Rajani et al. [41]. Although all the extrema have been described in the $\phi = 0.8$ case, obvious discrepancy could be found compared with the reference. On the contrary, coincidence is relatively poor in the $\phi = 0.6$ case. The difference among the schemes attenuates at $x/D = 1.54$ and 2.02.

However, the streamwise Reynolds stress $\langle u'u' \rangle$ (Fig. 21) and transverse Reynolds stress $\langle v'v' \rangle$ (Fig. 22) vary at several streamwise locations. In general, the fluctuations of $\phi = 0.6$ and $\phi = 0.8$ are larger than those of $\phi = 1.0$ as expected. The results of $\phi = 1.0$ are closer to the experimental results compared with its low-dissipation counterparts.

Although the low numerical dissipation method has certain advantages in the prediction of the turbulence structures in the far wake region, it may cause greater resolved eddy viscosity in the near-wall and near wake regions. As a result, the overall eddy viscosity might be inconsistent with the expectation due to the emergence of the aliasing error, and thus affects the calculation results. Therefore, the interaction between the truncation and aliasing errors should be taken into consideration under the current circumstances. The de-aliasing strategies might be implemented in the future researches to exclude the influences of aliasing errors, although additional computational cost is inevitable.

4.3 Flow over NACA0021 airfoil

Meanwhile, an example of airfoil at large angle of attack was also used to verify the accuracy of the method. The unsteady separated turbulence flow over NACA0021 airfoil in deep stall shows significant unsteady dynamics and is therefore a good test case for LES method [53]. In the present study, the angle of attack was set as 60°. The airfoil chord (c) and the freestream flow velocity (u_∞) were selected as the characteristic length and the reference velocity in this test case. Specifically, the flowfield around NACA0021 airfoil at $Re = 2.7 \times 10^5$ and $Ma = 0.1$ was simulated using the third-order IPDG method and LES dynamic subgrid model.
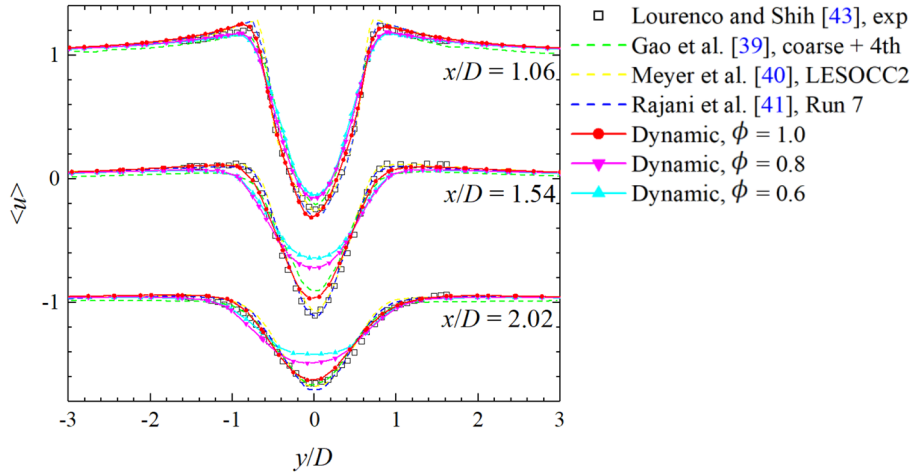
(a) In the near wake region
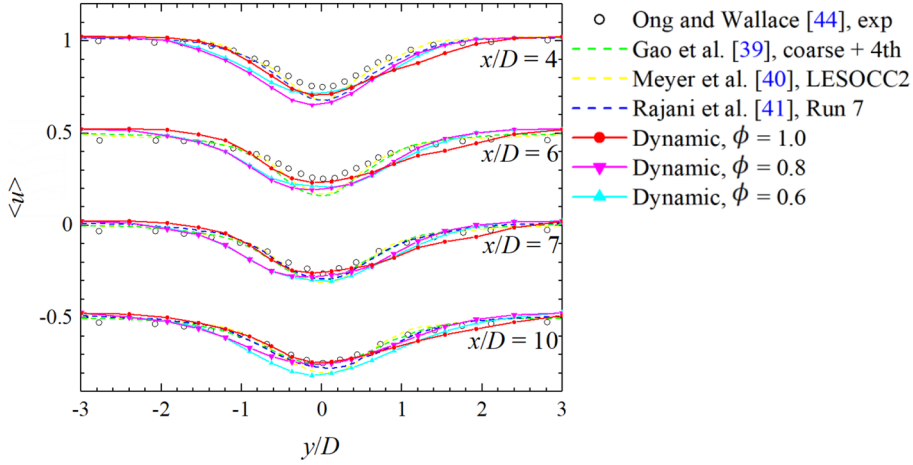
(b) In the far wake region

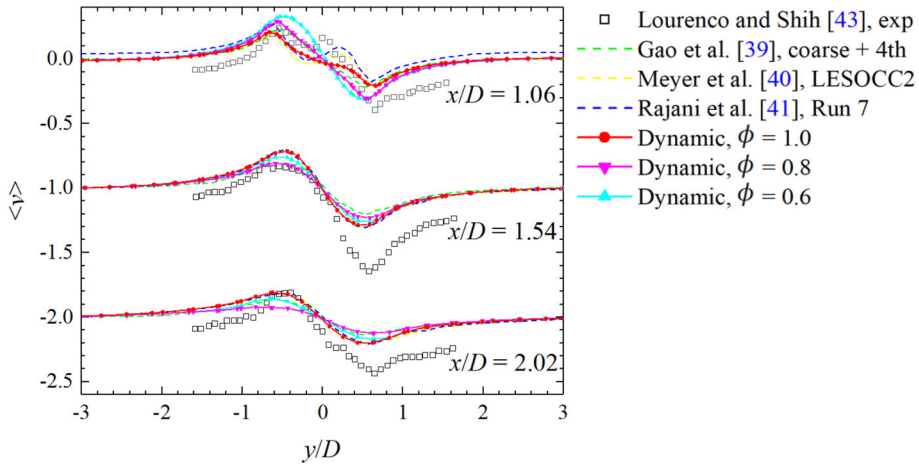**Fig. 18** Effect of numerical dissipation on mean streamwise velocity at different locations

Fig. 19 Effect of numerical dissipation on mean transverse velocity in the wake region
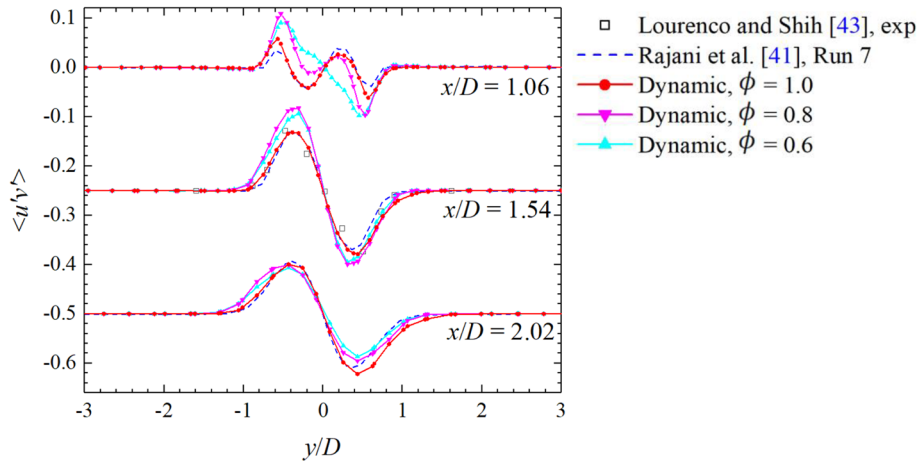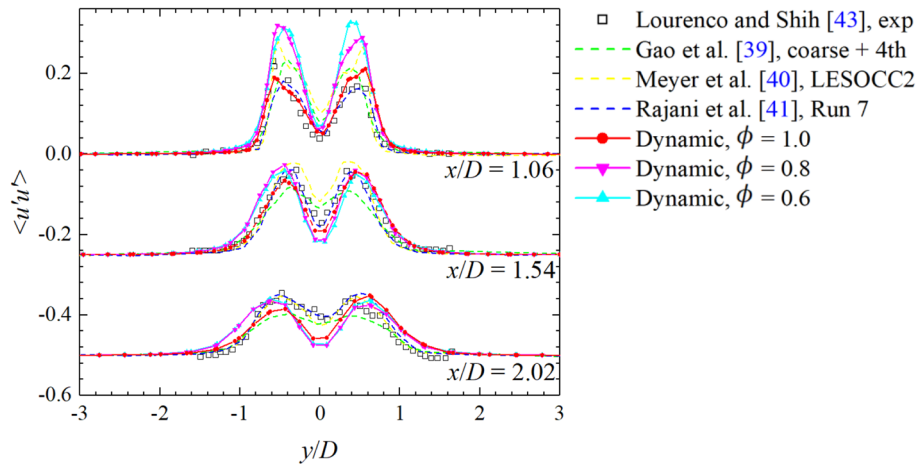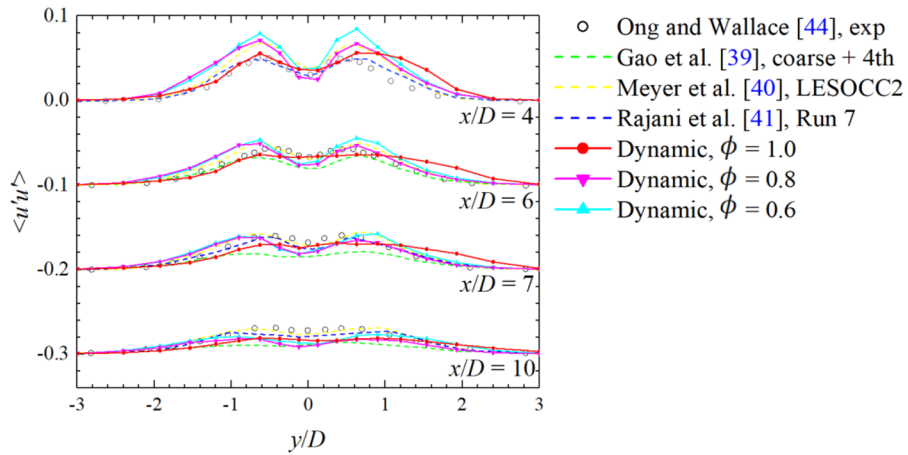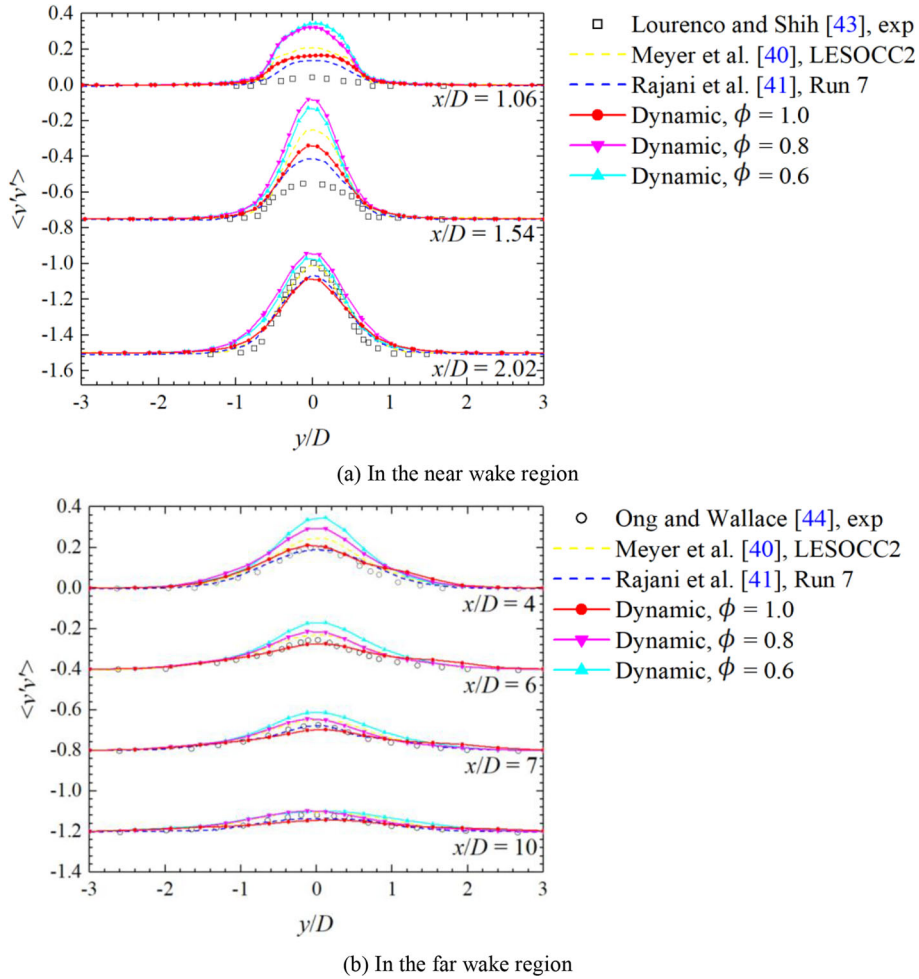
Fig. 20 Effect of numerical dissipation on Reynolds shear stress in the wake region

(a) In the near wake region

(b) In the far wake region

Fig. 21 Effect of numerical dissipation on streamwise Reynolds stress at different locations

Fig. 22 Effect of numerical dissipation on transverse Reynolds stress at different locations

A C-type structured grid system was generated around the airfoil. Likewise, x, y and z represent the streamwise, transverse and spanwise directions, respectively. There are 200 and 36 points in the circumferential and spanwise directions. 20 layers of body-fitted grids were generated on the airfoil with no-slip wall boundary condition, and the mesh has been refined in the vicinity of the wall surface to reach the requirement of $y^+ \approx$ 2. Periodic boundary conditions were adopted in the spanwise direction, and the spanwise length (L_z) is 0.5 c. The non-reflecting boundary condition was imposed on the far field, which is about 5 c away from the wall. Overall, the total number of grid elements is 0.5 M, as shown in Fig. 23. The non-dimensional time step of the simulation was set as $\Delta t = 0.005$ and the information within $T = 18$ has been collected for the time-averaged analysis.

Figure 24 plots the distributions of the pressure coefficient C_p on the pressure and suction surfaces of the airfoil. Note that C_p is averaged over time and the spanwise direction. The trend coincides with the experimental data [54] and the numerical results [53]. In detail, the result in the case of $L_z = 0.5c$ is even better than the reference result of $L_z = 1.0c$ [53]. The influence of airfoil span has not been discussed in the present study due to the limitation of the computational cost, which will be conducted in the near future.

Then, the time-averaged flow field information, including the distributions of the pressure and eddy viscosity, is shown in Fig. 25. Analogous distributions could be found in the references [55, 56]. The remarkable primary vortex behind the suction surface leads to the emergence of low-pressure region.

Furthermore, the distributions of turbulent field parameters are shown in Fig. 26 in terms of Reynolds stresses. It can be seen that the turbulent flow generation takes place far away from the wall surface. Combined with the streamline distribution in Fig. 25a, it can be found that the shape of vortex is well outlined. Both the
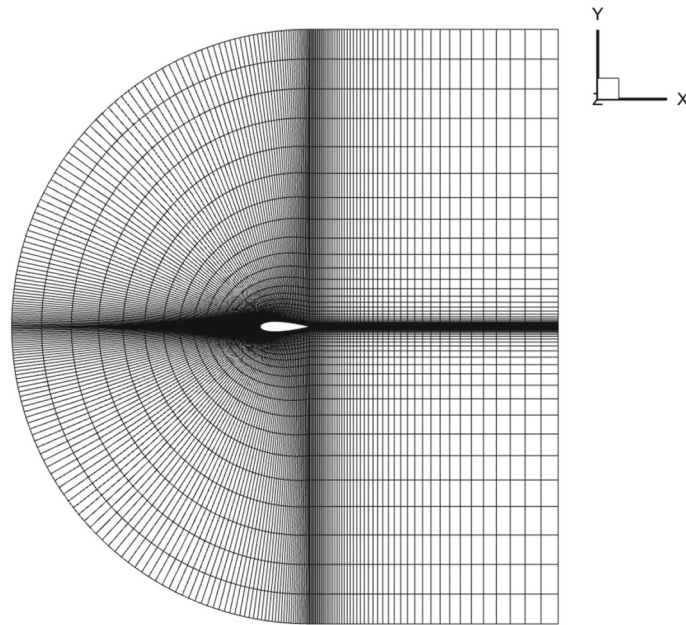
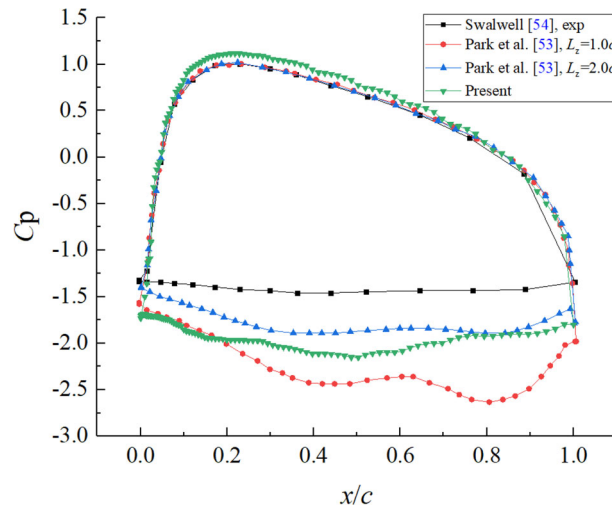**Fig. 23** Computational domain grid for NACA0021 airfoil

Fig. 24 C_p distributions on the pressure and suction surfaces

streamline or transverse Reynolds stress and the Reynolds shear stress have relatively high values near the profile of the vortex, which indicates that there are strong fluctuations and energy exchange.

Figure 27 plots the streamwise velocity spectrum at five positions in $z = 0.25c$ plane, the locations of which have been plotted in Fig. 26 by crosses and given in Fig. 27. The trends of changing are consistent, and the main shedding frequency can be clearly detected. The secondary shedding frequency is twice the main frequency. The present result of $L_z = 0.5c$ is similar to the result of $L_z = 1.0c$ in [53]. Increasing the spanwise length will probably give results closer to the experimental data. Based on the above cylinder and airfoil results, our IPDG method demonstrates satisfactory accuracy in the resolution of separation vortices in accompany with the dynamic subgrid model, and the turbulence field is accurately characterized. It will provide a powerful tool in the simulation of complex detached flow structures.
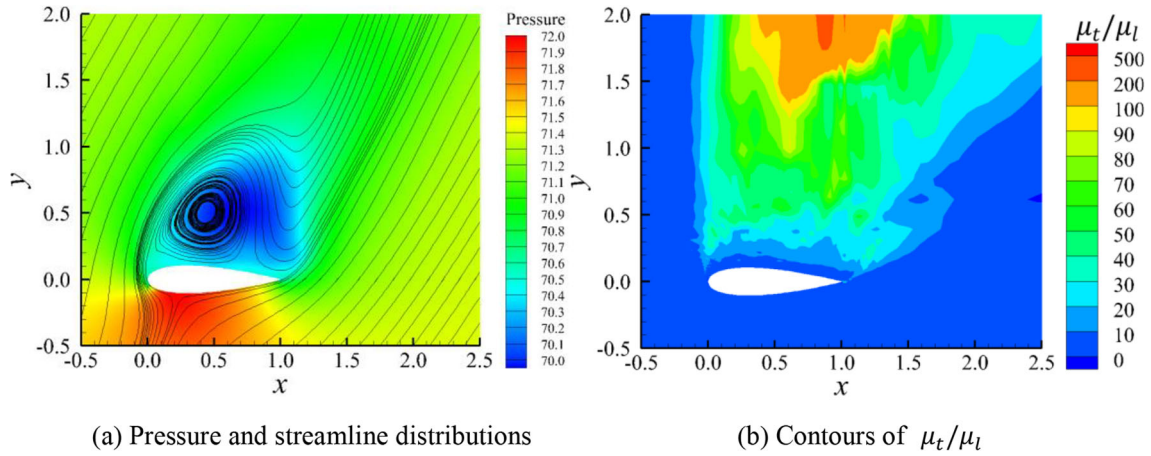
(a) Pressure and streamline distributions (b) Contours of μ_t/μ_l

**Fig. 25** Time-averaged flow field distribution

5 Conclusions

In this study, an improved IPDG method was adopted to conduct LES studies around cylinders and airfoils in accompany with various SGS models. From the numerical aspect, a lifting operator was introduced to prevent from the calculation of the homogeneity tensor. From the turbulence modeling aspect, a truncation process was adopted within the test filtering procedure when the coefficient was dynamically updated in the dynamic model. The influences of SGS models and numerical dissipation have been comprehensively discussed through a cylinder wake simulation at $Re = 3900$. The following conclusions could be drawn.

1. It has been validated that the improved IPDG method can reach a precision of at least fourth order. In the cylinder wake simulation, the accuracy was validated in terms of pressure distribution, velocity and Reynolds stress profiles. When the dynamic subgrid model was adopted, the performances according to flow separation and vortex shedding frequency are consistent with the references with a maximum error of -5.34%. Therefore, the modeled viscosity and dissipation characteristics of the present IPDG-LES framework have been verified.

2. The Smagorinsky model with a damping function, WALE, and dynamic subgrid models possess certain advantages over the original Smagorinsky model. Nevertheless, they do not consistently result in improved performance. In detail, the WALE model works well within the near-wall region, but the improvement is not evident in the wake region, leading to a relative error of -12.50% when bubble length is concerned. Actually, the modifications of the damping function and WALE model mainly focus on the boundary layer behaviors. In comparison, the dynamic subgrid model is constructed based on scale similarity and local flow information, which are also valid in the wake region. In this way, the dynamic subgrid model provides the best result.

3. LLF fluxes with three artificial dissipation terms have been adopted to discuss the influence of numerical dissipation. Accidentally, the original LLF flux could achieve the highest precision, which could be interpreted by the development of the resolved viscosity. With the suppression of numerical dissipation, the velocity fluctuation is greatly enlarged and the relative error of bubble length is drastically increased to more than -17.31%, which might be also attribute to the impact of the aliasing errors. To this end, the flux schemes should be delicately selected and the de-aliasing strategies should be implemented in the corresponding studies.

4. The ability to predict massive flow separation has also been validated through the NACA0021 airfoil flow simulation at $Re = 2.7 \times 10^5$ and $AOA = 60°$. Our results are in coincidence with the references in terms of static pressure, streamline and viscosity distributions. Moreover, the capability of turbulence description has also been validated by Reynolds stress distributions and streamwise velocity spectrum.
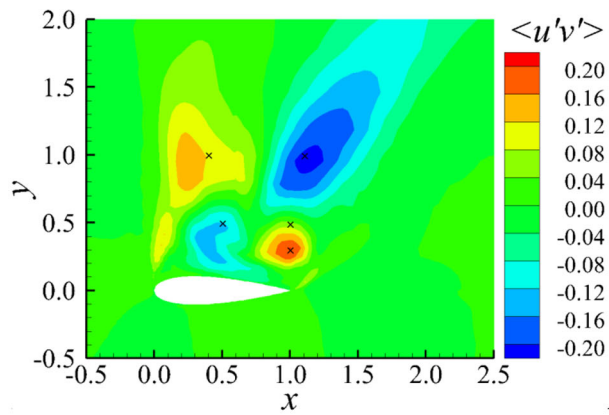
(a) Reynolds shear stress distribution
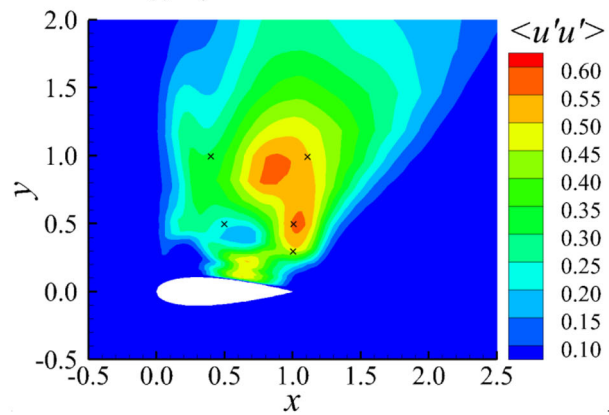
(b) Streamwise Reynolds stress distribution
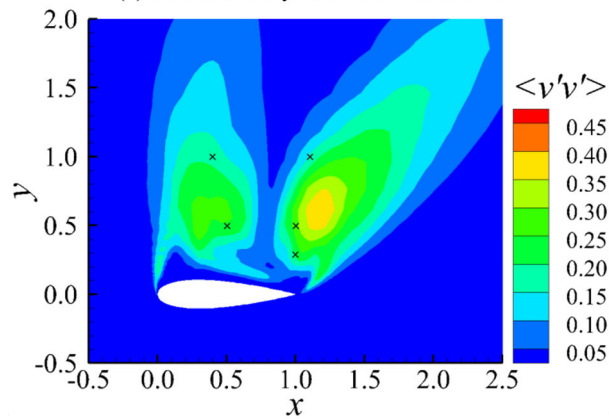
(c) Transverse Reynolds stress distribution

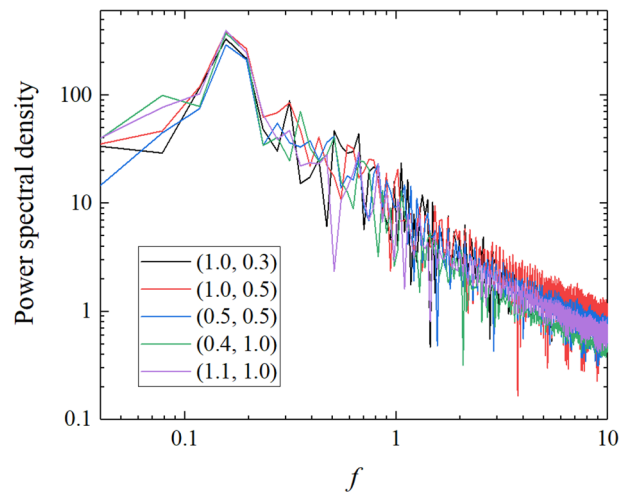**Fig. 26** Distributions of turbulence field parameters

Fig. 27 Streamwise velocity spectrum (the NACA0021 airfoil flow simulation)

Declarations

Conflict of interest The authors have no competing interests as defined by Springer, or other interests that might be perceived to influence the results and/or discussion reported in this paper.

Ethics approval and consent to participate All the authors mentioned in the manuscript have agreed for authorship, read and approved the manuscript, and given consent for submission and subsequent publication of the manuscript.

Consent for publication The manuscript has not been published before (except in the form of an abstract or as part of a published lecture, review or thesis). The manuscript will not be submitted elsewhere until the editorial process is completed. Its publication have been approved by all the authors.

References

1. Cockburn, B., Shu, C.W.: The local discontinuous Galerkin method for time-dependent convection-diffusion systems. SIAM J. Numer. Anal. **35**(6), 2440–2463 (1998)
2. Hartmann, R., Houston, P.: Symmetric interior penalty DG methods for the compressible Navier–Stokes equations I: method formulation. Int. J. Numer. Anal. Model. **3**(1), 1–20 (2006)
3. Hartmann, R., Houston, P.: Symmetric interior penalty DG methods for the compressible Navier–Stokes equations II: goal-oriented a posteriori error estimation. Int. J. Numer. Anal. Model. **3**(2), 141–162 (2006)
4. Abbà, A., Bonaventura, L., Nini, M., Restelli, M.: Dynamic models for large eddy simulation of compressible flows with a high order DG method. Comput. Fluids **122**, 209–222 (2015)
5. Bian, W., Zhao, Q., Zhao, G.: Low dissipation simulation for vortex flowfield of rotor in hover based upon discontinuous Galerkin method. Trans Nanjing Univ. Aeronaut Astronaut. **38**(6), 975–983 (2021)
6. Arya, N., De, A.: Effect of grid sensitivity on the performance of wall adapting SGS models for LES of swirling and separating-reattaching flows. Comput. Math. Appl. **78**(6), 2035–2051 (2019)

7. Lee, C.Y., Cant, S.: Assessment of LES subgrid-scale models and investigation of hydrodynamic behaviour for an axisymmetrical bluff body flow. Flow Turbul. Combust. **98**(1), 155–176 (2017)
8. Poncet, S., Viazzo, S., Oguic, R.: Large eddy simulations of Taylor–Couette–Poiseuille flows in a narrow-gap system. Phys. Fluids **26**(10), 1–27 (2014)
9. Yuen, A.C.Y., Yeoh, G.H., Timchenko, V., Cheung, S.C.P., Chen, T.: Study of three LES subgrid-scale turbulence models for predictions of heat and mass transfer in large-scale compartment fires. Numer. Heat Tranf. A Appl. **69**(11), 1223–1241 (2016)
10. Wang, R., Xiao, Z.L.: Reynolds-constrained large-eddy simulation: sensitivity to constraint and SGS models. In: Proceedings of the 7th Symposium on Hybrid RANS-LES Methods. Berlin, Germany (2020)
11. Bassi, F., Botti, L., Colombo, A., Crivellini, A., Ghidoni, A., Massa, F.: On the development of an implicit high-order discontinuous Galerkin method for DNS and implicit LES of turbulent flows. Eur. J. Mech. B. Fluids **55**, 367–379 (2016)
12. Bassi, F., Rebay, S.: A high-order accurate discontinuous finite element method for the numerical solution of the compressible Navier–Stokes equations. J. Comput. Phys. **131**(2), 267–279 (1997)
13. Bassi, F., Rebay, S., Mariotti, G.: A high-order accurate discontinuous finite element method for inviscid and viscous turbomachinery flows. In: Proceedings of the 2nd European Conference on Turbomachinery Fluid Dynamics and Thermodynamics (1997)
14. Arnold, D.N., Brezzi, F., Cockburn, B., Marini, L.D.: Unified analysis of discontinuous Galerkin methods for elliptic problems. SIAM J. Numer. Anal. **39**(5), 1749–1779 (2002)
15. Zhao, M., Wei, T., Hao, S., Ding, Q., Liu, W., Li, X., Liu, Z.: Turbulence simulations with an improved interior penalty discontinuous Galerkin method and SST k-ω model. Comput. Fluids **263**, 1–14 (2023)
16. Chapelier, J.B., de la Llave, P.M., Lamballais, E.: Development of a multiscale LES model in the context of a modal discontinuous Galerkin method. Comput. Methods Appl. Mech. Eng. **307**, 275–299 (2016)
17. Bassi, F., Colombo, A., Crivellini, A., Fidkowski, K.J., Franciolini, M., Ghidoni, A., Noventa, G.: Entropy-adjoint p-adaptive discontinuous Galerkin method for the under-resolved simulation of turbulent flows. AIAA J. **58**(9), 3963–3977 (2020)
18. Sengupta, K., Mashayek, F., Jacobs, G.B.: Large-eddy simulation using a discontinuous Galerkin spectral element method. In: Proceedings of the 45th AIAA Aerospace Sciences Meeting and Exhibit. Reno, Nevada (2007)
19. Tugnoli, M., Abbà, A., Bonaventura, L., Restelli, M.: A locally p-adaptive approach for large eddy simulation of compressible flows in a DG framework. J. Comput. Phys. **349**, 33–58 (2017)
20. Abbà, A., Recanati, A., Tugnoli, M., Bonaventura, L.: Dynamical p-adaptivity for LES of compressible flows in a high order DG framework. J. Comput. Phys. **420**, 1–21 (2020)
21. Nigro, A., De Bartolo, C., Crivellini, A., Franciolin, M., Colombo, A., Bassi, F.: A low-dissipation DG method for the under-resolved simulation of low Mach number turbulent flows. Comput. Math. Appl. **77**(6), 1739–1755 (2019)
22. Winters, A.R., Moura, R.C., Mengaldo, G., Gassner, G.J., Walch, S., Peiro, J., Sherwin, S.J.: A comparative study on polynomial dealiasing and split form discontinuous Galerkin schemes for under-resolved turbulence computations. J. Comput. Phys. **372**, 1–21 (2018)
23. van der Bos, F., Geurts, B.J.: Computational error-analysis of a discontinuous Galerkin discretization applied to large-eddy simulation of homogeneous turbulence. Comput. Methods Appl. Mech. Eng. **199**, 903–915 (2010)
24. Plata, M.D., Lamballais, E., Naddei, F.: On the performance of a high-order multiscale DG approach to LES at increasing Reynolds number. Comput. Fluids **194**, 1–19 (2019)
25. Kirby, R.M., Karniadakis, G.E.: De-aliasing on non-uniform grids: algorithms and applications. J. Comput. Phys. **191**(1), 249–264 (2003)
26. Beck, A.D., Flad, D.G., Tonhäuser, C., Gassner, G., Munz, C.D.: On the influence of polynomial de-aliasing on subgrid scale models. Flow Turbul. Combust. **97**(2), 475–511 (2016)
27. Zhang, T., Lu, H., Qin, W., Chen, Z.: High-order discontinuous Galerkin method for hovering rotor simulations based on a rotating reference frame. Trans. Nanjing Univ. Aeronaut Astronaut. **36**(1), 57–70 (2019)
28. Li, S.: Time advancement of the Navier–Stokes equations: p-adaptive exponential methods. J. Flow Control Meas. Visual. **8**(2), 63–76 (2020)
29. Smagorinsky, J.: General circulation experiments with the primitive equations. Mon. Weather Rev. **91**(3), 99–164 (1963)
30. Zhao, W., Wang, J., Cao, G., Xu, K.: High-order gas-kinetic scheme for large eddy simulation of turbulent channel flows. Phys. Fluids **33**(12), 1–19 (2021)
31. Piomelli, U., Zang, T.A., Speziale, C.G., Hussaini, M.Y.: On the large-eddy simulation of transitional wall-bounded flows. Phys. Fluids **2**(2), 257–265 (1990)
32. Germano, M., Piomelli, U., Moin, P., Cabot, W.H.: A dynamic subgrid-scale eddy viscosity model. Phys. Fluids **3**(7), 1760–1765 (1991)
33. Taher, A.B.H., Kanfoudi, H., Zgolli, R., Ennouri, M.: Investigation of subgrid-scale models in large eddy simulation on the unsteady flow around a hydrofoil using OpenFOAM. Iran. J. Sci. Technol. Trans. Mech. Eng. **44**(2), 465–480 (2020)
34. Nicoud, F., Ducros, F.: Subgrid-scale stress modelling based on the square of the velocity gradient tensor. Flow Turbul. Combust. **62**(3), 183–200 (1999)
35. Plata, M.D., Couaillier, V., le Pape, M.C.: On the use of a high-order discontinuous Galerkin method for DNS and LES of wall-bounded turbulence. Comput. Fluids **176**, 320–337 (2018)
36. Rusanov, V.V.: Calculation of interaction of nonsteady-shock waves with obstacles. J. Comput. Math. Phys. **1**, 267–279 (1961)
37. Li, Y.Z.: Large eddy simulation of flow around a cylinder at Re = 3900 using a CFD code. In: Proceedings of the International Conference on Civil Engineering and Transportation. Jinan, China (2015)
38. Norberg, C.: An experimental investigation of the flow around a circular cylinder: influence of aspect ratio. J. Fluid Mech. **258**, 287–316 (1994)
39. Gao, R., Yu, J., Kong, W., Yan, C.: Evaluation of a WENO method in implicit large eddy simulation of circular cylinder flow. In: Proceedings of the 2nd International Conference on Computer and Automation Engineering (ICCAE). Singapore (2010)

40. Meyer, M., Hickel, S., Adams, N.A.: Assessment of implicit large-eddy simulation with a conservative immersed interface method for turbulent cylinder flow. Int. J. Heat Fluid Flow **31**(3), 368–377 (2010)
41. Rajani, B.N., Kandasamy, A., Majumdar, S.: LES of flow past circular cylinder at Re $=$ 3900. J. Appl. Fluid Mech. **9**(3), 1421–1435 (2016)
42. Ouvrard, H., Koobus, B., Dervieux, A., Salvetti, M.V.: Classical and variational multiscale LES of the flow around a circular cylinder on unstructured grids. Comput. Fluids **39**(7), 1083–1094 (2010)
43. Lourenco, L.M., Shih, C.: Characteristics of the plane turbulent near wake of a circular cylinder. A particle image velocimetry study (data taken from [45])
44. Ong, L., Wallace, J.: The velocity field of the turbulent very near wake of a circular cylinder. Exp. Fluids **20**(6), 441–453 (1996)
45. Fröhlich, J., Rodi, W., Kessler, P., Parpais, S., Bertoglio, J.P., Laurence, D.: Large eddy simulation of flow around circular cylinders on structured and unstructured grids. In: Ernst Heinrich Hirschel, editor, Numerical Flow Simulation I, volume 66 of Notes on Numerical Fluid Mechanics (NNFM). Springer, Berlin (1998)
46. Kravchenko, A.G., Moin, P.: Numerical studies of flow over a circular cylinder at ReD $=$ 3900. Phys. Fluids **12**(2), 403–417 (2000)
47. Ferrer, E.: An interior penalty stabilised incompressible discontinuous Galerkin–Fourier solver for implicit large eddy simulations. J. Comput. Phys. **348**, 754–775 (2017)
48. Chow, F.K., Moin, P.: A further study of numerical errors in large-eddy simulations. J. Comput. Phys. **184**(2), 366–380 (2003)
49. Klein, M., Freitag, M., Janicka, J.: Numerical determination of the scaling exponent of the modeled subgrid stresses for eddy viscosity models. In: Proceedings of the Symposium on Complex Effects in Large Eddy Simulation. Lemesos, Cyprus (2007)
50. Xiao, Z.X., Liu, J., Huang, J.B., Fu, S.: Numerical dissipation effects on massive separation around tandem cylinders. AIAA J. **50**(5), 1119–1136 (2012)
51. Meyers, J.: Accuracy of large-eddy simulation strategies. Ph.d. thesis, Katholieke Universiteit Leuven, Belgium (2004)
52. Lysenko, D.A., Ertesvag, I.S., Rian, K.E.: Large-eddy simulation of the flow over a circular cylinder at Reynolds number 3900 using the OpenFORM toolbox. Flow Turbul. Combust. **89**(4), 491–518 (2012)
53. Park, J.S., Witherden, F.D., Vincent, P.E.: High-order implicit large-eddy simulations of flow over a NACA0021 aerofoil. AIAA J. **55**(7), 1–12 (2017)
54. Swalwell, K.E.: The effect of turbulence on stall of horizontal axis wind turbines. Ph.d. thesis, Department of Mechanical Engineering, Monash University, Melbourne, Australia (2005)
55. Du, L., Ning, F.F.: Scale adaptive simulation of flows past an airfoil after stall. In: Proceedings of the ASME Fluids Engineering Division Summer Meeting (FEDSM). Rio Grande, Puerto Rico (2012)
56. Guseva, E.K., Garbaruk, A.V., Strelets, M.K.: Assessment of delayed DES and improved delayed DES combined with a shear-layer-adapted subgrid length-scale in separated flows. Flow Turbul. Combust. **98**(2), 481–502 (2017)